An Improved Side-Slither Relative Radiometric Calibration Method for WFV Satellite: Taking HY1D CZI as an Example

Ru Chen, Mi Wang, *Member, IEEE*, Yingdong Pi, Tao Peng, Rongfan Dai, and Ru Wang

***Abstract*—Wide field of view (WFV) push-broom optical satellites can acquire ground images over hundreds to thousands of kilometers in a single pass, thanks to their large field of view (FOV) cameras consisting of tens or even hundreds of thousands of detectors, which also makes their relative radiometric correction (RRC) difficult. Existing side-slither-based RRC approaches overlook the distinct structural design of WFV push-broom optical satellite cameras, thus failing to rectify nonlinear distortions in side-slither images stemming from the nonflat arrangement of camera detectors. Furthermore, these methods necessitate the corresponding pixels (pixels of the same ground object) covering the entire FOV in side-slither images. However, the brief duration of side-slither imaging makes it unfeasible to cover the entire FOV with calibration data. To address these issues, we propose a novel RRC approach for WFV push-broom optical satellites, achieved based on a thorough analysis of the unique structural traits of WFV push-broom optical cameras, enabling precise standardization of the nonlinear distortions in side-slither data. Additionally, a local-to-global side-slither calibration strategy is proposed to obviate the requirement for corresponding pixels to cover the entire FOV in calibration data. Experiments using the Haiyang-1D Coastal Zone Imager satellite indicate that our method effectively rectified nonlinear distortions in side-slither data, and evident RRC accuracy improvement with that of the existing methods can be obtained.**

***Index Terms*—Haiyang-1D coastal zone imager (HY-1D CZI), relative radiometric calibration (RRC), side-slither, wide field of view (WFOV).**

I. Introduction

REMOTE-SENSING satellites have become an indispensable means of acquiring extensive ground information, with the quality of their image products largely depending on the design of the optical imaging system and subsequent radiometric calibration. Nowadays, charge-coupled devices (CCDs) are frequently integrated into optical imaging systems, offering push-broom and whisk-broom imaging modes as alternatives. In practice, push-broom optical sensors are predominant in this field. Linear array push-broom sensors are composed of a group of independent detectors. When provided with the same radiance input, the detectors should ideally yield identical digital number (DN) outputs. However, due to factors, such as overall sensor circuit design and detector manufacturing processes, detector responses are not consistent, resulting in visible stripes in the imagery (see Fig. 1). The process of rectifying and compensating for inconsistencies between detector responses is referred to as relative radiometric calibration (RRC), which is an important processing procedure to improve the quality of optical satellite images [1].

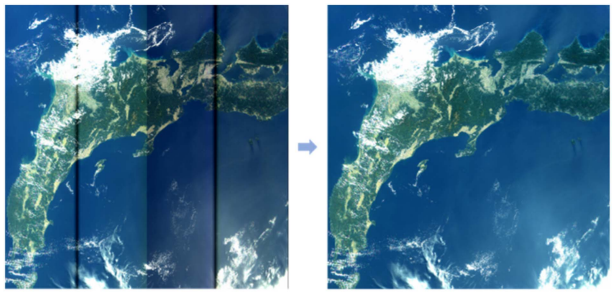

(a) (b)

Fig. 1. (a) Raw image of HY-1D CZI with stripe noise and (b) image after relative radiometric calibration.

The essence of RRC is a map linking the noisy signals of the detector outputs to the noise-free signals. For push-broom optical sensors, RRC methods can be broadly classified into four groups [2]: laboratory RRC, on-board RRC, uniform-field RRC, and statistical RRC. Laboratory RRC relies on integrating spheres to generate standardized signals, with the integration sphere utilized as input and the sensor as output to calculate RRC coefficients [3]. However, this method is not applicable to on-orbit satellite data due to changes in device status after launch. On-board RRC [4] employs standard light sources (built-in lamps, the sun, and the moon) to construct standardized signals and establish response relationships, but on-board calibration devices are complex, bulky, and expensive, and introduce calibration errors due to aging. In uniform-field RRC [5], standardized signals are constructed from uniform terrain, with large-area ocean, ice, and desert imagery used to

Manuscript received 9 February 2024; revised 13 April 2024 and 30 April 2024; accepted 12 May 2024. Date of publication 20 May 2024; date of current version 14 June 2024. This work was supported in part by the National Key Research and Development Program of China Under Grant 2022YFB3902804 and in part by the National Natural Science Foundation of China Major Program under Grant 42192583. *(Corresponding authors: Mi Wang; Yingdong Pi.)*

Ru Chen, Mi Wang, Yingdong Pi, Tao Peng, and Ru Wang are with the State Key Laboratory of Information Engineering in Surveying, Mapping and Remote Sensing, Wuhan University, Wuhan 430079, China (e-mail: chenru@whu.edu.cn; wangmi@whu.edu.cn; pyd_imars@whu.edu.cn; pengtao@whu.edu.cn; wangr2017@whu.edu.cn).

Rongfan Dai is with the School of Cyber Science and Engineering, Wuhan University, Wuhan 430079, China (e-mail: dairongfan@whu.edu.cn).

Digital Object Identifier 10.1109/JSTARS.2024.3402812

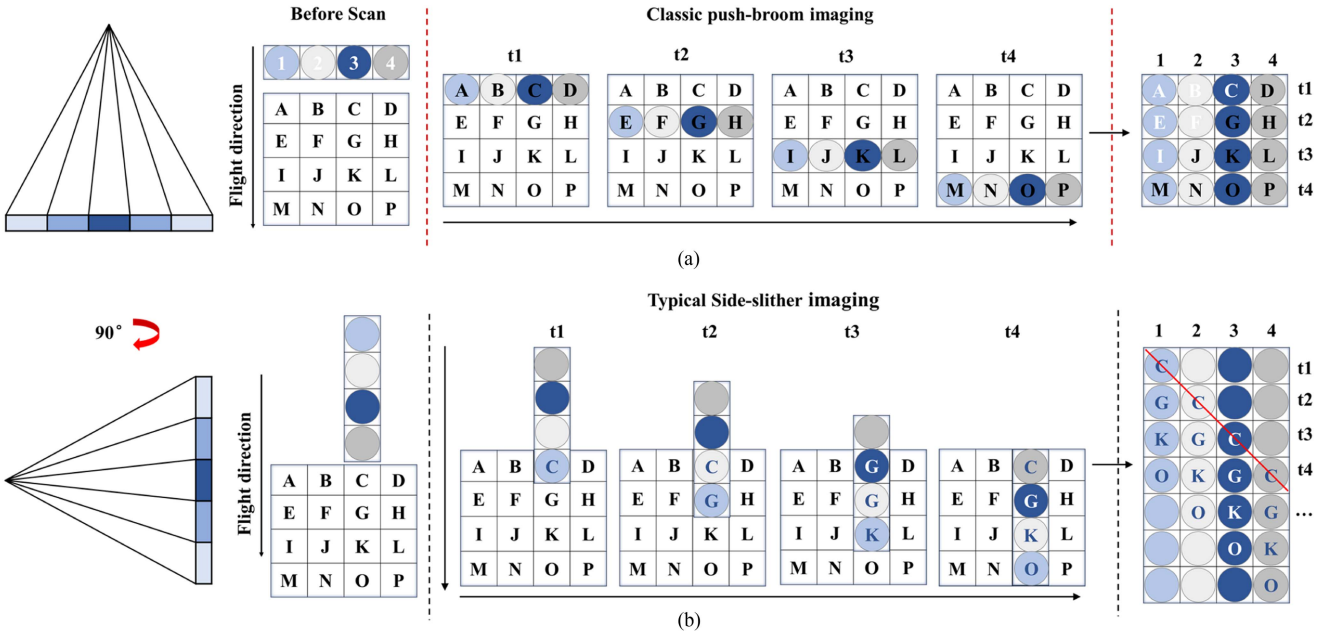

Fig. 2. Comparison of (a) typical push-broom imaging and (b) typical side-slither imaging.

establish relative relationships between detectors during satellite operation [6], [7]. However, this method has stringent requirements with respect to terrain uniformity, which are often difficult to fulfill. Statistical RRC [8], [9] weakens the influence of random factors through data accumulation, relying on the law of large numbers to construct standardized signals. The quality of this method's calibration depends on the richness and duration of the accumulated data, making it probabilistic and requiring long statistical periods that result in low timeliness. In addition to these methods, Moghimi et al. [10] propose a robust algorithm for relative radiometric normalization (RRN) of bitemporal multispectral images. Vicarious techniques are employed to enhance the relative radiometric quality of images [11], [12], [13]. Lunar radiometric calibration is utilized to capture long-term trends and monitor satellites for inconsistencies [14]. Furthermore, pseudoinvariant calibration sites are utilized for the radiometric calibration and temporal stability monitoring of optical satellite sensors [15]. Methods, such as the random sample consensus-based RRN method [16] and the support vector machine regression-based model [17], are also implemented to improve image radiometric quality. Additionally, the block adjustment method [18], [19] is employed to eliminate radiometric differences between multiple sensors.

With the development of satellites equipped with agile maneuvering capabilities, side-slither imaging mode has become a reliable approach to address inconsistent detector responses. By rotating the camera and adjusting the yaw angle, all detectors pass sequentially over the same location, mitigating the influence of factors, such as sunlight, atmosphere, and topography. The QuickBird [20] satellite employs the side-slither imaging mode and exploits the satellite's agility, resulting in consistent pixel inputs for each camera's detectors. The AMETHIST method was first tested on the Pleiades satellite [21], [22]. Similarly, the GaoFen-9 [23], [24] and Landsat-8 [25], [26] satellites have adopted the approach of rotating the camera by 90° to perform RRC, with promising results. Since this method does not depend on ground or uniform calibration scenes, high calibration accuracy and strong timeliness are ensured.

Fig. 2 [24] reveals the imaging process during a yaw maneuver of a conventional linear array push-broom satellite camera. When the satellite platform rotates by 90°, the arrangement direction of the camera detectors becomes parallel to the satellite's flight direction, and each detector images the same ground object in sequence. The detector at the forefront of the flight direction images the ground object first, while those at the rear image it with a certain delay. Furthermore, a currently imaging detector is from the first one, the more delayed its imaging time is for the same ground object, resulting in a greater row-direction offset of its line image relative to the line image of the first detector. Therefore, the pixel position relationships of images of the same ground object captured by all sensor detectors cannot be used directly for calibration. Side-slither images must undergo normalization processing to ensure that the line images produced by all detectors have no offset in the row direction.

It can be observed that the offset of each detector's image is directly proportional to its center distance from the first detector. For the conventional linear array push-broom satellite cameras, the size of the detectors is uniform, and they are arranged in a straight line closely together. When the camera is in the yaw imaging mode, the arrangement direction of the detectors is parallel to the flight direction, and the center distance between adjacent detectors in the flight direction is equal to the size of the detectors themselves. Therefore, the offset of the line images produced by adjacent detectors in the row direction is equal, and the image offset of each detector relative to the first detector (referred to as the detector image offset) is a linear function of their center distance relative to the first detector (referred to as the detector center distance). Side-slither-based RRC requires

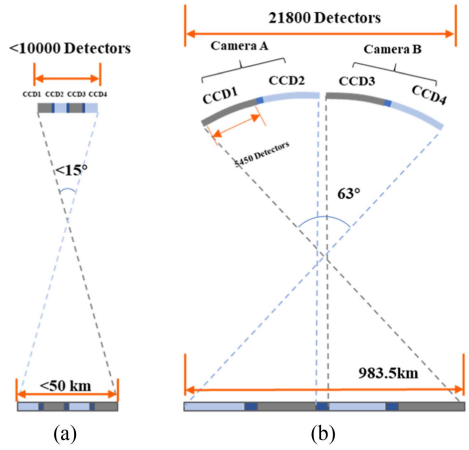

Fig. 3. Typical narrow FOV sensor structural design for (a). HY-1D CZI: sensor structural design for (b).

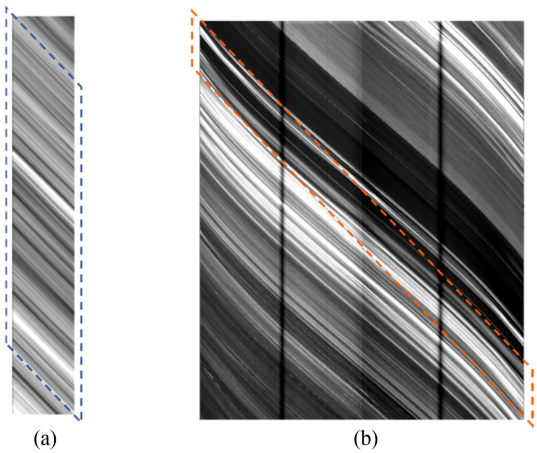

Fig. 4. Comparison of a typical narrow FOV side-slither image (linear feature) for (a) and HY-1D CZI side-slither image (curve feature) for (b), with corresponding pixels in dotted boxes, respectively.

correcting this diagonal line such that it is horizontal, thus ensuring that the pixels in each image row represent imaging information of the same ground feature. This process is referred to as the standardization or normalization of side-slither data. The core of yaw image normalization is to calculate the image offset of each detector, which can be accurately obtained through line detection methods, achieving high-precision normalization processing of yaw images.

Based on the linear features of side-slither data, several standardization methods have been proposed. Pesta et al. [25] introduced a method that corrects the image using a 45° inclination angle. Zhang and Li [27], among others, employed a least significant difference-based method [28] to detect diagonal lines within side-slither data by performing a statistical analysis to determine the optimal slope and subsequently calculating the offsets for each column of the image. Li et al. [29] further optimized the process by incorporating sensor geometric correction principles, resulting in more accurate standardized side-slither data.

In the case of wide field of view (WFV) linear array push-broom optical satellites, in which the FOV can exceed 60°, the typical linear detector layout can result in significant geometric distortions, as the central and peripheral detectors will differ substantially in their principal distance. To ensure a more consistent distribution of principal distances among detectors, WFV linear array push-broom sensors often adopt a nonlinear detector arrangement. This design is employed by Haiyang-1D coastal zone imager's (HY-1D CZIs) sensor [see Fig. 3(b)], resulting in a remarkable FOV of 63°.

However, during side-slither imaging, a nonflat sensor arrangement introduces variations in the effective dimensions of the detectors along the scan direction and unequal center-to-center distances between detectors. Consequently, the diagonal features of the corresponding pixels that manifest in side-slither images change from linear to curved, as shown in Fig. 4. Existing side-slither data standardization methods based on linear features cannot be directly applied to WFV satellites.

Another issue is that the traditional side-slither-based RRC methods generally necessitate corresponding pixels covering the entire FOV, discarding the "upper triangle" and "lower triangle"

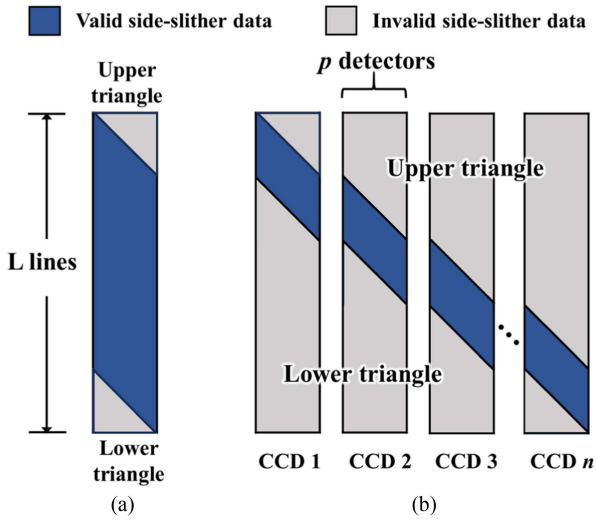

Fig. 5. Comparison of typical narrow FOV side-slither RRC data utilization and WFV side-slither RRC data utilization.

of the images. While this strategy is acceptable for detectors with a narrow FOV, as the discarded portions constitute a relatively small percentage of the entire side-slither data [see Fig. 5(a)], it poses challenges for satellite sensors with ultra-WFV imaging, as these sensors often consist of multiple CCDs stitched together, with hundreds of thousands of sensor detectors. To ensure stable on-orbit operation of the satellite, the side-slither imaging duration is generally short such that the number of captured data rows may be smaller than the total number of sensor detectors. This situation results in an image width that is larger than or equal to the image height, with hardly any corresponding pixels covering the entire FOV, as shown in Fig. 5(b). In such cases, achieving high-precision RRC coefficients using typical side-slither RRC methods becomes extremely challenging.

To address these issues, we developed a novel side-slither RRC method based on a thorough analysis of the unique structural traits of WFV push-broom optical cameras and culminating in polynomial correction models enabling precise

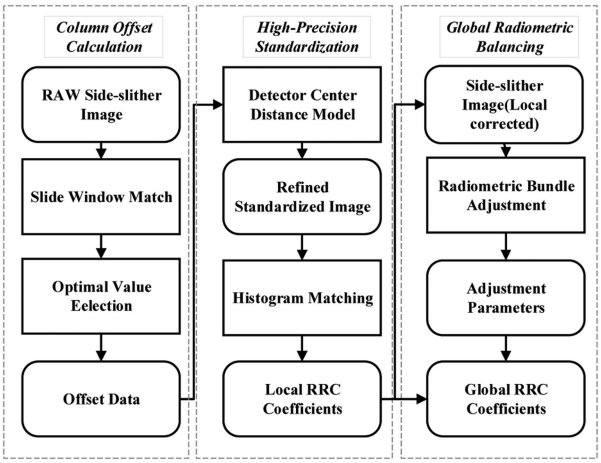

Fig. 6. Workflow of our proposed radiometric calibration method for HY-1D CZI side-slither data.

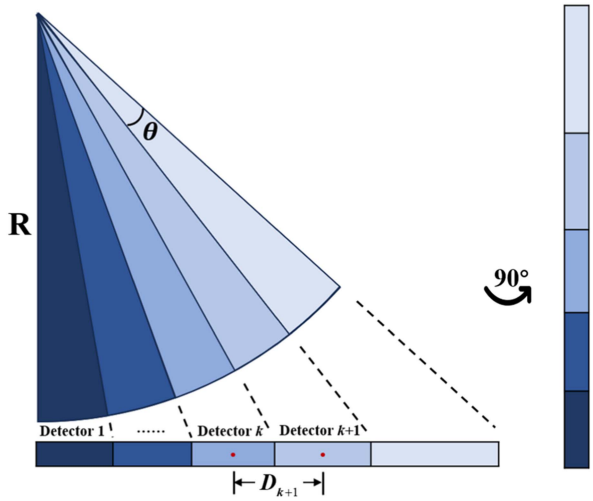

Fig. 7. Analysis of the HY-1D CZIs detector arrangement.

standardization of the nonlinear distortions in side-slither data that arise due to nonflat detector arrangements. Additionally, overlapping information [30], [31], [32] from multiple CCDs within the camera was used to devise a strategy for local-to-global side-slither calibration. This approach obviates the requirement for corresponding pixels in calibration data to cover the entire FOV. We then compared our method with the typical side-slither RRC and statistical calibration methods using the HY-1D CZI satellite. The outcomes were assessed by visual examination and using calibration metrics.

The rest of this article is organized as follows. Section II describes both the workflow of the methods employed in this study and details of the calibration approach. Section III presents the experimental dataset and quantitative evaluation metrics, and outlines the comparative experiments, conducted using both the proposed and alternative methods, as well as the results of the visual assessments and quantitative indicators across all tested methods. Section IV discusses issues identified during the experiments. Finally, Section V concludes this article.

II. Methodology

A. Overview

The workflow of our proposed radiometric calibration method for HY-1D CZIs side-slither data is illustrated in Fig. 6.

Our method can be divided into two parts: local and global calibration. Given the new features of HY-1D CZIs side-slither data, our proposed standardization method transforms the bent diagonal line into a horizontal line to ensure that the images collected by all detectors are mutually consistent. As the upper and lower triangular parts of each CCD are invalid for RRC, in the standardization of side-slither data, they are discarded as a preprocess of local calibration. Local processing aims at eliminating the response differences of detectors in their respective CCDs, which guarantees the internal radiometric quality of the CCDs. After local calibration, the response differences between detectors within each CCD are removed, but the response differences between CCDs remain. A full FOV adjustment for radiometric calibration is, therefore, performed to achieve color consistency.

B. Standardization of the Side-Slither Image

The raw calibration data must be standardized or regularized such that all DNs in each row direction of the standardized image are the DNs captured by all detectors.

1) Detector Center Distance Model: As mentioned in Section I, the image offset of each detector is directly proportional to its center distance from the first detector. The HY-1D CZI sensor adopts a free-form surface design, each detector corresponds to an equal central angle at the focal point, which maintains the principal distances between the central and edge detectors as consistent as possible. Thus, instead of arranging the detectors in a straight line, they are arranged in an approximate circular arc. The offset characteristics of the side-slither data are highly dependent on the distance between the centers of the detectors. To facilitate the analysis of offset characteristics, the curved arrangement of detectors is equivalently transformed into a traditional linear arrangement of detectors, as shown in Fig. 7.

As the field of view (FOV) increases, the equivalent size of detectors on the focal plane gradually increases, and the distance between adjacent detectors also increases with the expansion of the FOV. This implies that with the increase in the FOV, the detector displacement between neighboring detectors also gradually increases. In the yaw image, detectors from adjacent detectors capturing the same object form a curved line instead of a straight line such that ways to fit the new shape of the data were needed, as shown in Fig. 8.

On the free-form surface, the central angle (θ) between a single detector and the focus is considered. For the kth detector in the equivalent linear arrangement, its equivalent size is given as follows:

$$\text{Size}_k = R(\tan k\theta - \tan(k-1)\theta) \tag{1}$$

where R represents the camera's focal length, and Size_k represents the kth detector's equivalent size.

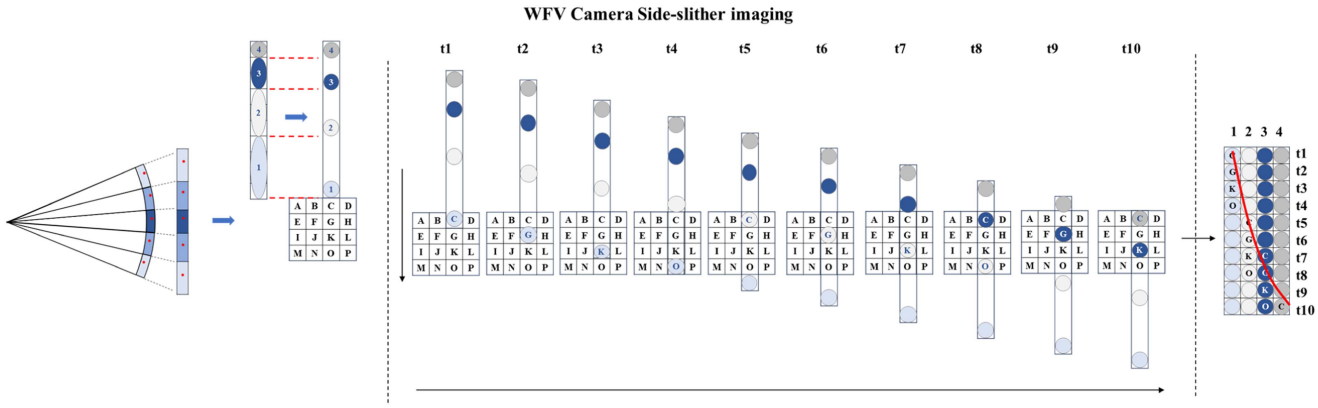

Fig. 8. WFV satellite camera side-slither imaging.

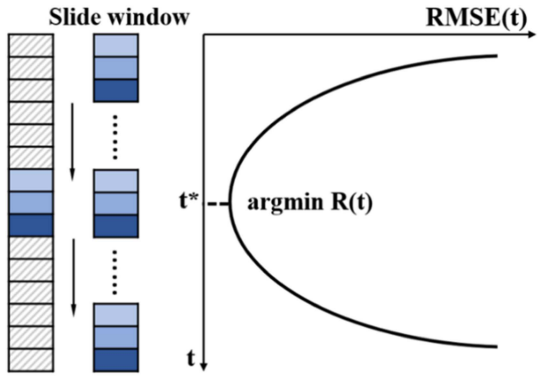

Fig. 9. Calculation of adjacent column offset based on sliding window RMSE.

The distance between the center of the $(k+1)$th detector and the kth detector is expressed as follows:

$$\begin{aligned} D_{k+1} &= \frac{\text{Size}_{k+1} + \text{Size}_k}{2} \\ &= \frac{\tan(k+1)\theta - \tan k\theta + \tan k\theta - \tan(k-1)\theta}{2} \cdot R \\ &= \frac{\tan(k+1)\theta - \tan(k-1)\theta}{2} \cdot R. \end{aligned} \tag{2}$$

Considering errors introduced by the yaw angle, and mismatches between the camera's integration time and the satellite's ground speed, the image offset of the k+1th detector relative to the kth detector can be expressed through a more detailed mathematical model

$$S_{k+1} = \lambda \left[\tan(k+1)\theta - \tan(k-1)\theta\right] \tag{3}$$

where λ represents the compensation for yaw angle, camera integration time, satellite ground speed, and the principal moment of the camera.

2) Column Offset Calculation: Taking column j of the image I (size $m \times n$) as an example, the offset of column $j+1$ relative to column j is calculated. First, a certain number of rows (e.g., L rows) of data are selected starting from the ith row of column j to be used as the reference column vector V_j (4)

$$V_j = [I(i,j), I(i+1,j), I(i+2,j), \ldots, I(i+L-1,j)]. \tag{4}$$

Assuming a search radius of r in the row direction, on column $j+1$ of the image, starting from the $(i-r)$th row, consecutive L rows of data are selected as the target-matching column vector. This process continues until the $(i-r+L)$th row, forming a set of target-matching column vectors (5)

$$\begin{aligned} \left\{V_{j+1}^t = [[I(i,j+1), I(i+1,j+1), I(i+2,j+1), \ldots,\right. \\ \left. I(i+t,j+1)]] \,|t \in [-r,r]\right\}. \end{aligned} \tag{5}$$

The RMSE between V_j and V_{j+1}^t named $R_{j+1}(t)$ can be calculated, as shown in the following equation:

$$\begin{aligned} &R_{j+1}(t) \\ &= \sqrt{\frac{\sum_{l=0}^{L-1} \left[\text{DN}(I(i+t+l,j+1)) - \text{DN}(I(i+l,j))\right]^2}{L}}. \end{aligned} \tag{6}$$

In (6), $\text{DN}(I(i,j))$ represents the DN value of the image at the ith row and jth column. If t^* is the value of t that minimizes $R_{j+1}(t)$, (see Fig. 9) then the offset S_{j+1} between the column $j+1$ and the column j of the image is equal to t^* and is represented, as shown in the following equation:

$$\begin{cases} t^* = \arg\min_{t\in[-r,r]} R_{j+1}(t) \\ S_{j+1} = t^*. \end{cases} \tag{7}$$

Combining (3) and (7), it is possible to solve the parameter λ.

After the relative offsets for all columns in the image are calculated, the global offset for column j (G_S_j) of the image (see Fig. 10) is obtained, as shown in the following equation:

$$G\_S_j = \sum_{j=1}^{N} S_j. \tag{8}$$

Equations (3) and (7) are used to solve for the parameter λ, considering that (3) is a tangent function, its Taylor expansion is generally used for subsequent fitting calculations in practice.

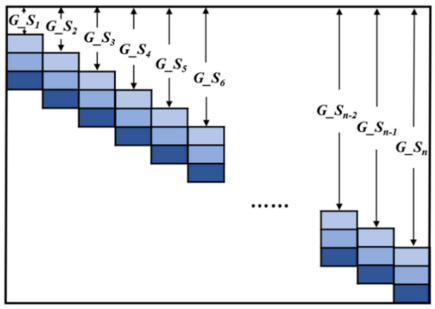

Fig. 10. Calculation of global offset for each column.

The Taylor series expansion of $\tan k$ is shown as follows:

$$\tan k = k + \frac{k^3}{3} + \frac{2k^5}{15} + \frac{17k^7}{315} + \cdots. \tag{9}$$

Here, up to the fifth term, the center-to-center distance D_{k+1} between the kth and $(k+1)$th detectors can be represented by a quintic polynomial (10)

$$D_{k+1} = q_0 + q_1 k + q_2 k^2 + q_3 k^3 + q_4 k^4 + q_5 k^5. \tag{10}$$

The logical relationship between the detector number (column index j) and the offset in the column direction (Offset(j)) can also be expressed by a quintic polynomial (11)

$$\text{Offset}(j) = a_0 + a_1 j + a_2 j^2 + a_3 j^3 + a_4 j^4 + a_5 j^5. \tag{11}$$

The offset values calculated using (8) are fitted to obtain polynomial parameters $[a_0, a_1, a_2, a_3, a_4, a_5]$ according to (11). After the fitting process, the offset values are obtained, and the original side-slither data are rearranged as a group of horizontal lines using the following equation:

$$I_{\text{std}}(i, j) = I(i + \text{offset}(j), j). \tag{12}$$

The use of a quintic polynomial model to fit the obtained offsets and the standardization of side-slither data can effectively eliminate errors introduced by the RMSE-based method. This process provides a dependable calibrated data source for subsequent calculations of relative radiometric coefficients.

C. Local Calibration

After standardization, each row of the slide-slither image can be regarded as if it were obtained by all detectors photographing the same feature. To calibrate the response difference between detectors, each CCD is treated as an independent unit and each detector's response difference is calibrated using the sum of the histogram of its CCD as an expectation histogram.

The expectation histogram of each CCD is calculated by summing the histograms of all of its detectors. When the amount of statistical data is sufficient, based on the law of large numbers, the influence of random errors, such as those in terrain and illumination, will gradually be eliminated, while systematic errors between detectors will remain. Local calibration coefficients can be generated by matching each detector's histogram to the expected histogram of its CCD. The purpose of local calibration is to eliminate systematic errors between detectors in a single CCD, and then level up radiometric vignetting in overlaps to avoid introducing unreliable radiometric information during full

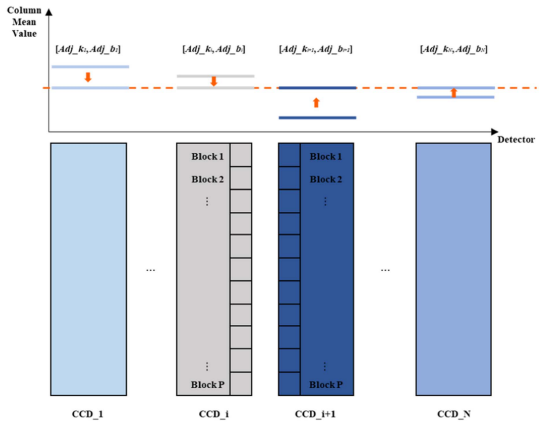

Fig. 11. Full FOV adjustment for each CCD.

FOV adjustment. The calculation process is described in detail in related works [24], [43].

D. Full FOV Adjustment

Based on the local radiometric calibration coefficients of the side-slither data of individual CCDs, an RRC is applied to the original side-slither data. The RRC eliminates the influence of random errors and inconsistencies among detectors within each CCD. However, differences in response between CCDs remain. HY-1D CZI consists of two cameras, with two CCDs per camera, and uses optical butting and FOV butting between cameras. However, due to the minimal displacement in the FOV stitching between cameras, the four CCDs can effectively be treated as collinear CCDs. Based on a linear correction model [34], [35], [36] utilizing the overlapping information from the side-slither data of the four CCDs, a least-squares adjustment model is established [32] to solve the adjustment parameters for each CCD. By combining the local radiometric calibration coefficients of all CCDs, the global radiometric calibration coefficients are computed.

For example, in the case of two adjacent CCDs, Li et al. [37] used the mean and standard deviation as expressions of the radiometric information for overlapping regions. Due to the limited duration of side-slither data acquisition, it is often challenging to obtain image data that cover the entire sensor's grayscale range uniformly. In our method, images of each overlapping region are divided into blocks along the row direction and their means are then calculated as expressions of the radiometric information for the overlapping regions, as shown in Fig. 11. Compared with the use of only the mean and standard deviation, our method increases the number of observations in the adjustment equations, thereby enhancing the reliability of parameter estimation.

The adjustment parameters for the ith CCD (out of a total of N CCDs) are set to $(\text{Adj\_}k_i, \text{Adj\_}b_i)$. Before adjustment, the mean DN value of the Pth block in the ith left overlap is $L\_M_i^P$. The purpose of the adjustment (13) is to make the DN values of each overlapping region consistent

$$\sigma_{M_i^P} = L\_M_i^P \cdot \text{Adj\_}K_i + \text{Adj\_}B_i - (R\_M_i^P \cdot \text{Adj\_}K_{i+1} + \text{Adj\_}B_{i+1}) \tag{13}$$

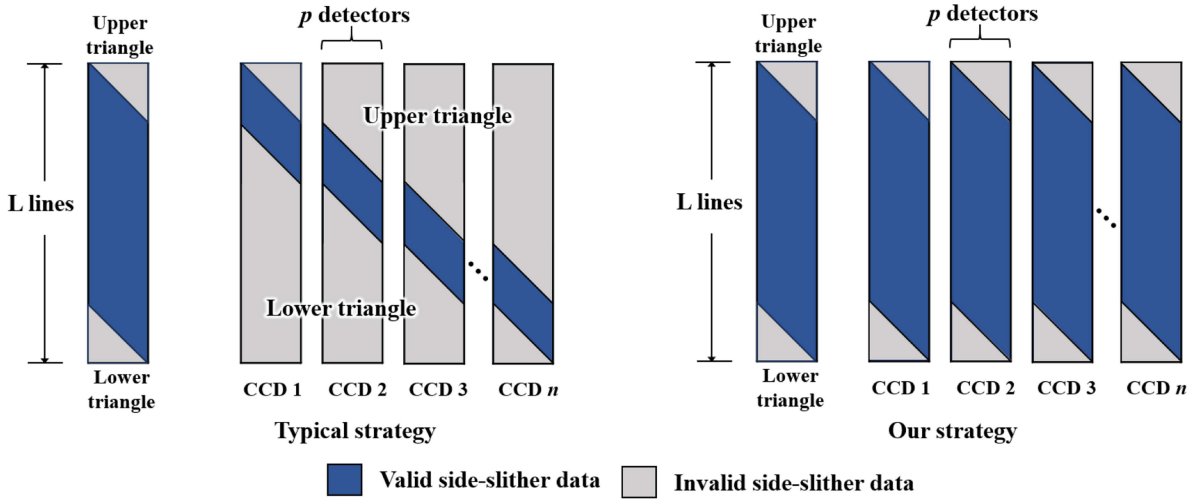

Fig. 12. Comparison of typical side-slither RRC data utilization and the proposed RRC data utilization.

where $\sigma_{M_i^p}$ represents the difference between the DN values of the *P*th block in the *i*th left overlap and the DN values of the *P*th block in the *i*th right overlap.

A constraint is, therefore, incorporated to minimize the loss of radiometric information after the adjustment for each block, with the aim of keeping the change in the standard deviation of the block ($\sigma_{\mathrm{Std}_i^P}$) before and after adjustment as small as possible (14)

$$\sigma_{\mathrm{Std}_i^p} = \mathrm{Std}_i^P \cdot \mathrm{Adj}\_k_i - \mathrm{Std}_i^P \tag{14}$$

where Std_i^P represents the DN value's standard deviation of the *P*th block in the *i*th overlap.

This process yields the adjustment (15), (16), (17), and (18)

$$\begin{bmatrix} \sigma_{O_1} \\ \sigma_{O_2} \\ \vdots \\ \sigma_{O_{N-1}} \end{bmatrix} = \begin{bmatrix} O_1 & & & \\ & O_2 & & \\ & & \ddots & \\ & & & O_{N-1} \end{bmatrix} \begin{bmatrix} \mathrm{Adj}\_k_1 \\ \mathrm{Adj}\_b_1 \\ \mathrm{Adj}\_k_2 \\ \mathrm{Adj}\_b_2 \\ \vdots \\ \mathrm{Adj}\_k_N \\ \mathrm{Adj}\_b_N \end{bmatrix} - \begin{bmatrix} L_{O_1} \\ L_{O_2} \\ \vdots \\ L_{O_{N-1}} \end{bmatrix} \tag{15}$$

where O_i, σ_{O_i}, and L_{O_i} refer to

$$O_i = \begin{bmatrix} L\_M_i^1 & 1 & R\_M_i^1 & -1 \\ L\_\mathrm{Std}_i^1 & 0 & 0 & 0 \\ 0 & 0 & R\_\mathrm{Std}_i^1 & 0 \\ \vdots & \vdots & \vdots & \vdots \\ L\_M_i^P & 1 & R\_M_i^P & -1 \\ L\_\mathrm{Std}_i^P & 0 & 0 & 0 \\ 0 & 0 & R\_\mathrm{Std}_i^P & 0 \end{bmatrix} \tag{16}$$

$$\sigma_{O_i} = \begin{bmatrix} \sigma_{M_i^1} & \sigma_{L\_\mathrm{Std}_i^1} & \sigma_{R\_\mathrm{Std}_i^1} & \cdots & \sigma_{M_i^1} & \sigma_{M_i^1} & \sigma_{R\_\mathrm{Std}_i^P} \end{bmatrix}^T \tag{17}$$

$$L_{O_i} = \begin{bmatrix} 0 & L\_\mathrm{Std}_i^1 & R\_\mathrm{Std}_i^1 & \cdots & 0 & L\_\mathrm{Std}_i^P & R\_\mathrm{Std}_i^P \end{bmatrix}^T \tag{18}$$

where $L\_\mathrm{Std}_i^P$ represents the DN value's standard deviation of the *P*th block in the *i*th left overlap, and $R\_\mathrm{Std}_i^P$ represents the DN value's standard deviation of the *P*th block in the *i*th right overlap.

For sensors composed of multiple CCDs that are stitched together, our method does not require discarding all parts of the image that do not cover the entire FOV, as shown in Fig. 12. Compared with related processing methods [24], [29], [38], our approach significantly improves the utilization of side-slither data and avoids the distortion of radiometric correction parameters caused by insufficient inclusion of side slither in the calculations.

E. Global Calibration

With the lookup table generated for the *i*th CCD in the local calibration process, denoted as $\mathrm{LUT}_i(\mathrm{DN})$, and the adjustment parameters obtained for the *i*th CCD in the global least-squares adjustment process, represented as $[\mathrm{Adj}\_k_i, \mathrm{Adj}\_b_i]$, the global relative radiometric correction coefficient is given by the following equation:

$$\mathrm{Coef}_i(\mathrm{DN}) = \mathrm{int}\left(\mathrm{LUT}_i(\mathrm{DN})\right) \cdot \mathrm{Adj}\_k_i + \mathrm{Adj}\_b_i \tag{19}$$

where $\mathrm{Coef}_i(\mathrm{DN})$ represents the *i*th detector's global relative radiometric coefficients.

III. Experiment and Results

A. Parameters of HY-1D CZI

The coastal zone imager (CZI) aboard the HY-1D satellite consists of two three-mirror anastigmat cameras. Each of these cameras has a focal plane composed of two CCDs optically stitched together. These two cameras use field stitching, resulting in a combined total FOV angle of approximately 63°, meeting the

TABLE I
PARAMETERS OF HY-1D CZI

Parameter	Value
Spectral range	B1:0.42—0.50 μm
	B2:0.52—0.60 μm
	B3:0.61—0.69 μm
	B4:0.76—0.89 μm
Resolution	50 m
Field of View (FOV)	63°
Swath Width	983.5 km
Quantization	12bit
Orbit Height	782 km

TABLE II
LOCATIONS REPRESENTED BY THE EXPERIMENTAL DATASET

Name	Central Lat	Central Lon	Landcover	Note
Data-0	15°59'49.0"N	53°47'52.5"E	/	Side-slither Data, Passing through Iran, Saudi Arabia, etc.
Data-1	42°34'52.9"N	118°19'26.5"E	Land	North China Plain, China
Data-2	30°59'22.7"N	138°59'20.2"E	Sea	Philippine Sea, near Japan
Data-3	73°02'34.1"N	33°58'37.7"W	Snowfield	Greenland

requirement for a 950 km swath width and providing a ground resolution of 50 m (see Table I).

B. Parameters of the Experimental Dataset

Side-slither data captured in 2021 were selected for data standardization and RRC coefficient calculation. Additionally, four sets of image data captured in push-broom mode from the same year were used for validation. The side-slither data covered a geographic region extending from Iran and the Arabian Peninsula to the Indian Ocean, encompassing a variety of land cover types, including desert and ocean (see Fig. 13).

The validation data were captured (see Table II) over three locations: Greenland, North China Plain, and the Philippine Sea. These areas comprise various typical land cover types, including snowfields, land, and ocean, thus allowing verification of the radiometric calibration performance across high-, medium-, and low-sensor DN values.

C. Quality Assessment

Streaking metrics [39] can be used to evaluate the high-frequency response difference of adjacent detectors, as shown in the following equation:

$$\text{Streaking}_i = \frac{\left| m_i - \frac{m_{i-1}+m_{i+1}}{2} \right|}{\frac{m_{i-1}+m_{i+1}}{2}} \times 100\% \tag{20}$$

where Streaking_i is the streaking metric of the ith column and m_i is the mean value of the ith column.

The root mean square (RMS) [29], [40], [41] of the column mean of the image can be used to evaluate the low-frequency response difference of all detectors, as shown in the following equation:

$$\text{RMS} = \frac{\sqrt{\frac{\sum_{i=1}^{N}(m_i - m_{\text{img}})^2}{N-1}}}{m_{\text{img}}} \times 100\% \tag{21}$$

where m_i is the mean value of the ith column, m_{img} is the mean value of the entire image, and N is the column count.

D. Experiment Using Side-Slither Data

Typical methods of side-slither data standardization typically use the line segment detector (LSD) approach [29], [40]. However, for data from structures with unique design characteristics, such as the HY-1D CZI, the side-slither images will exhibit curved features instead of the typical straight lines, as shown in Fig. 14(a). The LSD-based standardization method struggles to align images with the same features within a single row, as depicted in Fig. 14(b). Our approach considers the curved design of the HY-1D CZI sensor and combines the neighboring column's RMSE with a third-degree polynomial model to accurately derive the offsets for each column. This achieves highly precise standardization of side-slither data, aligning images with the same features within the same row, as illustrated in Fig. 14(c).

Fig. 15(a) and (b), respectively, shows the standardized side-slither images obtained by direct application of the column offset calculation and after optimization using the detector center distance model. It can be observed that the standardized image using direct column offset calculation exhibits "jaggies" due to calculation errors and the propagation of errors in the column direction. In contrast, the standardized image using the detector center distance model establishes a theoretical correspondence between pixel numbers and detector offsets. By accurately fitting the actual detector offsets with a polynomial, the occurrence of "jaggies" is avoided.

Fig. 16(a) illustrates the full-field CZI side-slither image. Unlike the images obtained from the traditional sensors, the CZI side-slither image contains more prominent curve features, which is particularly evident in the red portion of Fig. 15(a) on the edge CCDs. After a second round of side-slither data standardization based on the traditional linear characteristics, the diagonal features caused by the 90° yaw angle are eliminated, leaving behind the curve distortion introduced by the sensor's inherent structural design, as depicted in Fig. 16(b). Building upon this foundation, in conjunction with the detector center distance model (see Section II-B), the accurate standardized side-slither calibration data can be obtained, as shown in Fig. 16(c).

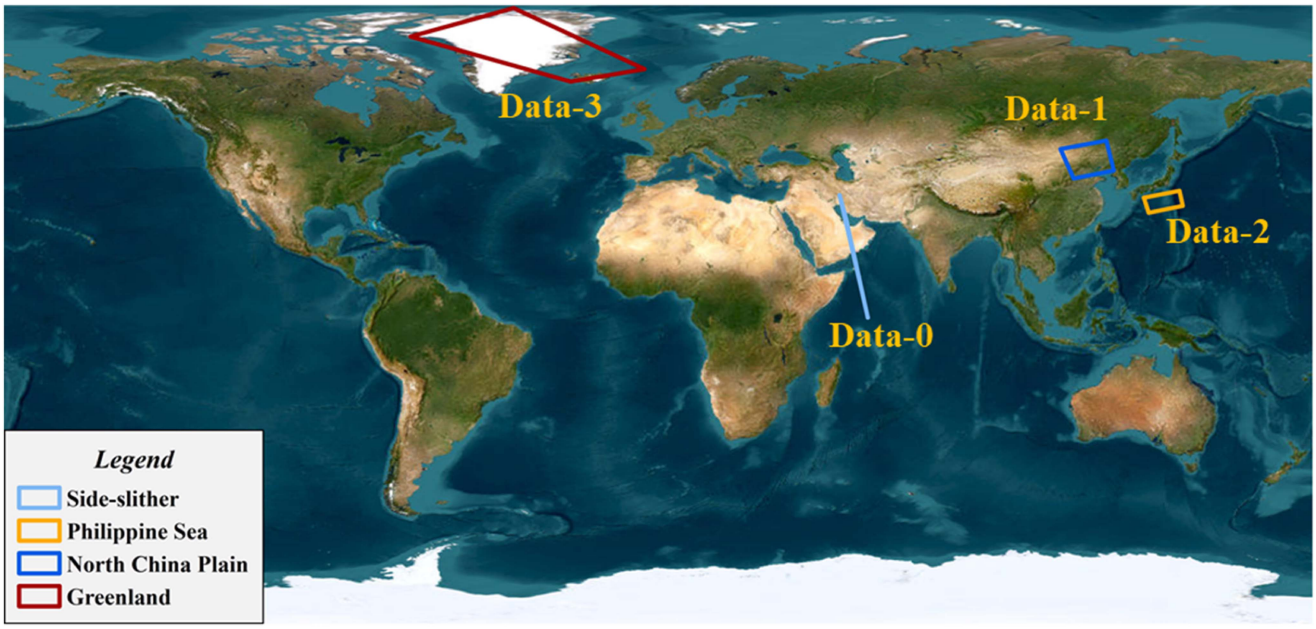

Fig. 13. Locations of the experimental dataset.

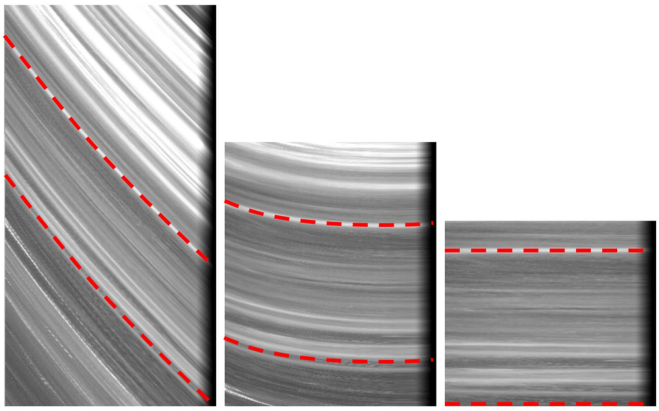

Fig. 14. Comparison of (a) HY-1D CZI raw image (local FOV of a single CCD) and standardized calibration images using the (b) LSD method and (c) our method.

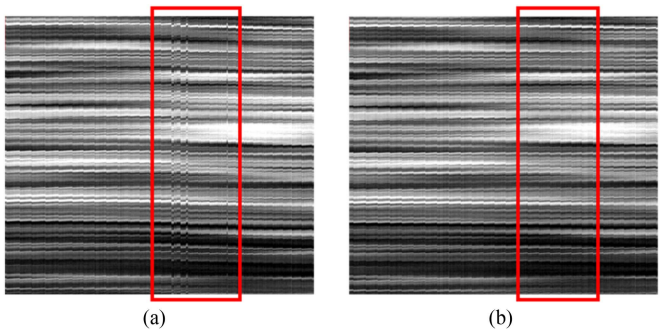

Fig. 15. Comparison of (a) HY-1D CZI standardized side-slither image (column offset calculation) and (b) standardized side-slither image using detector center distance model method.

After standardization of the side-slither data, local radiometric correction coefficients can be generated for each CCD. Subsequently, the overlapping information among the CCDs is used to establish a least-squares adjustment equation to calculate the parameters describing the transformation of local-to-global radiometric correction coefficients. The effectiveness of the radiometric correction coefficients was tested using the original side-slither images, as shown in Figs. 17, 18, and 19.

The visual assessment revealed the correction effects of the local radiometric calibration coefficients in the vignetting and nonvignetting regions. From Fig. 18(a) and (b), it is evident that the vignetting caused by optical sensor obstruction was effectively recovered in the image. Similarly, Fig. 18(c) and (d) shows that the striping noise caused by inconsistent detector responses was effectively eliminated from the image. The correction effects of the original image using both local and global radiometric calibration coefficients are presented in Fig. 17. Fig. 17(b) shows that the local radiometric coefficients effectively mitigated the radiometric inconsistency within a single CCD, and Fig. 17(c) shows that the global adjustment parameters effectively addressed the radiometric inconsistency across multiple CCDs.

As seen in Table III, after RRC, the average streaking in the corrected images decreased from 0.168 (B), 0.121 (G), 0.083 (R), and 0.103 (NIR) to 0.009 (B), 0.005 (G), 0.005 (R), and 0.003 (NIR). Maximum streaking decreased from 17.097 (B), 20.565 (G), 17.581 (R), and 17.237 (NIR) to 0.280 (B), 0.307 (G), 0.333 (R), and 0.311 (NIR). The standard deviation of streaking decreased from 0.261 (B), 0.277 (G), 0.236 (R), and 0.231 (NIR) to 0.014 (B), 0.006 (G), 0.008 (R), and 0.004 (NIR). The quantitative data also confirmed effective reduction of the detector response inconsistency in the side-slither images.

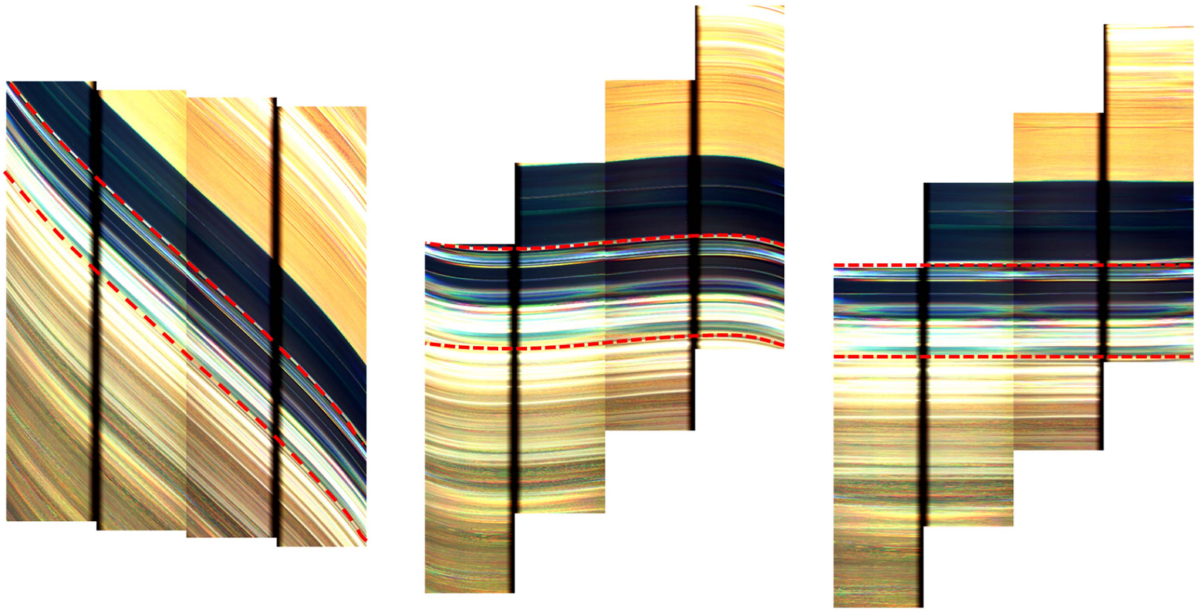

Fig. 16. Comparison of (a) HY-1D CZI raw image (full FOV) and standardized calibration images using the (b) LSD method and (c) our method.

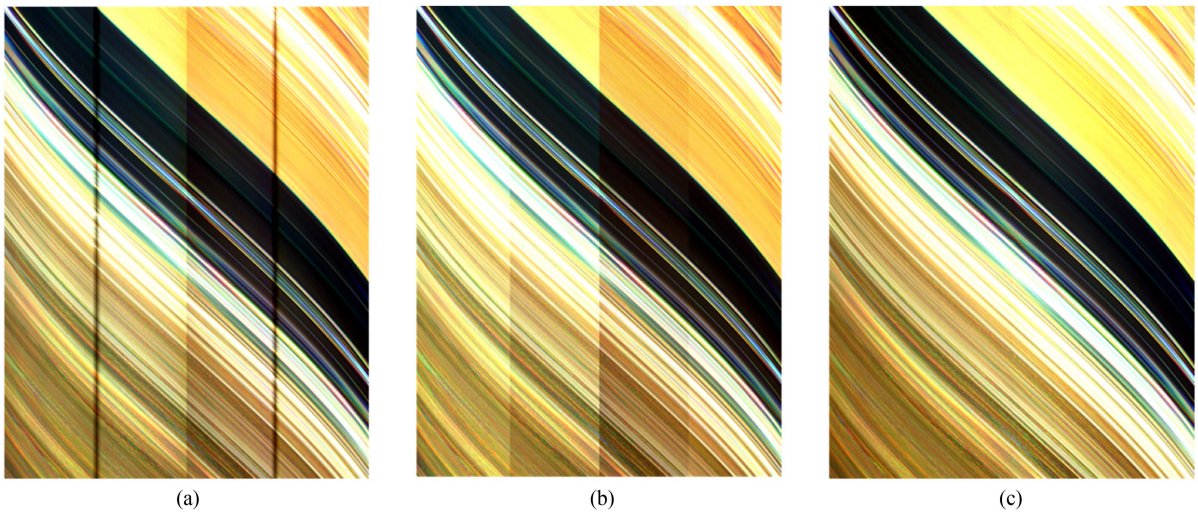

Fig. 17. (a) Original side-slither image, (b) side-slither image corrected with local radiometric coefficients, and (c) side-slither image corrected with global radiometric coefficients.

E. Experiment Using Typical Push-Broom Imaging Data

We conducted experimental comparisons using laboratory coefficients [3], the on-orbit statistical method [8], [14], the LSD-based method [19], [30], and the proposed method. According to the visual assessment, both the on-orbit statistical method and the proposed method achieved excellent results for land scenes (see Figs. 20 and 23). However, the method based on laboratory coefficient still resulted in noticeable striping artifacts and color discrepancies between CCDs. The LSD-based method generally performs well; however, there is a slight unnatural transition in the inter-CCD regions. Figs. 21 and 24 show that, for sea scenes, the laboratory coefficient method was not effective in adjusting the overall color differences of the images, and the prominent stripe noise persisted. However, both the proposed method and the on-orbit statistical method demonstrated better consistency in the overall color radiance, while the proposed method performed slightly better than the on-orbit statistical method in transition areas among multiple CCDs. The LSD-based method performs well in the transitions between CCDs, but there are relatively obvious striped flaws on the right side of the image. Notably, Figs. 22 and 25 show that, for snow scenes, the images corrected using the proposed method displayed the highest level of overall color consistency and the least amount of stripe noise and were, thus, clearly superior to the images obtained using the other methods. Although the on-orbit statistical method outperformed the laboratory coefficient method in achieving the overall color consistency, residual stripe errors

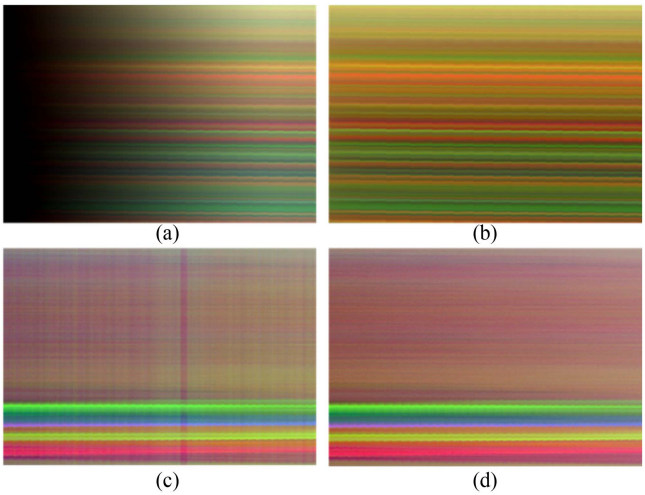

Fig. 18. (a) Original vignetting region image, (b) corrected vignetting region image, (c) corrected nonvignetting region image, and (d) original nonvignetting region image. All images were subjected to standardization processing.

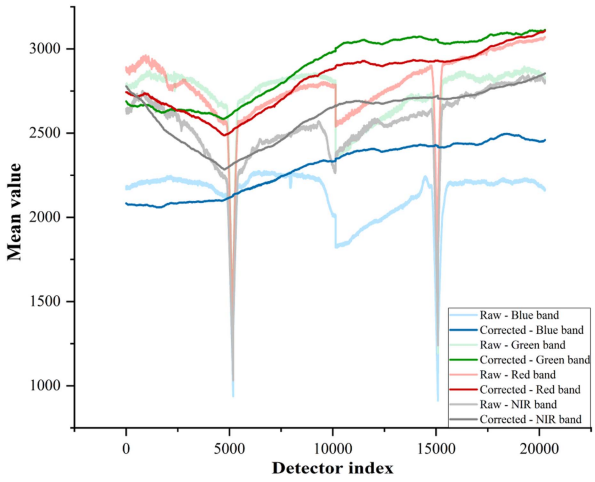

Fig. 19. Distribution of the average DN values of the side-slither image column.

TABLE III
STEAKING METRICS OF THE SIDE-SLITHER IMAGE BEFORE AND AFTER CORRECTION

Band	Method	Streaking_ Mean	Streaking_ Max	Streaking_S td
Band-1	Raw	0.168	17.097	0.261
	Proposed	**0.009**	**0.280**	**0.014**
Band-2	Raw	0.121	20.565	0.277
	Proposed	**0.005**	**0.307**	**0.006**
Band-3	Raw	0.083	17.581	0.236
	Proposed	**0.005**	**0.333**	**0.008**
Band-4	Raw	0.103	17.237	0.231
	Proposed	**0.003**	**0.311**	**0.004**

The bold entities are used to the best indicators.

could still be seen in the corrected images. Moreover, the LSD-based method exhibits noticeable overexposure in snow scenes, and the right side of the image has lost a lot of detail.

For the quantitative evaluation, Tables IV–VI present the parameters of the streaking coefficients and the RMS values of the image column mean for both the original normalized images and the relatively corrected images. Streaking coefficients offer insight into the level of pixel-scale stripe noise (high-frequency stripe noise) present in the images, while RMS values of the image column mean provide a measure of the color differences at various scales, such as between CCDs or even across the entire scene (low-frequency stripe noise).

For the high-frequency image stripe noise, in land scenes (medium radiance), all methods effectively reduced the radiometric nonuniformity relative to the original images (see Table IV). The best results were obtained with the proposed method and the on-orbit statistical method, with almost identical effects seen for the three streaking coefficient parameters. On average, streaking relative to the original images was reduced by 76% (B), 64% (G), 50% (R), and 60% (NIR). Maximum streaking was reduced by 98% (B), 91% (G), 95% (R), and 96% (NIR), while the standard deviation of the streaking value decreased by 86% (B), 83% (G), 74% (R), and 79% (NIR). Both the proposed method and the on-orbit statistical method were better than the laboratory coefficient method, by an average of 10%, in terms of average streaking, maximum streaking, and the standard deviation of streaking. The LSD-based method generally performs well, although it is slightly inferior to onboard statistics and the proposed method in terms of the maximum streaking metrics.

In sea scenes (low radiance), the performance of the proposed method and the on-orbit statistical method was again superior, reducing streaking relative to the original images by 75% (B), 54% (G), 35% (R), and 17% (NIR) on average. Maximum streaking was reduced by 84% (B), 75% (G), 54% (R), and 85% (NIR), and the standard deviation of streaking by 28% (B), 83% (G), 74% (R), and 79% (NIR). As in the other scenes, the laboratory coefficient method was inadequate for the sea scenes, with the maximum reduction in streaking limited to 9% in the R band and 15% in the NIR band compared with the original images, indicating significant residual stripe patterns in the corrected images. The LSD-based method performs poorly in the R band, with the striping coefficient metrics significantly lagging behind those of onboard statistics and the proposed method.

In the snow scenes (high radiance), the proposed method clearly outperformed the other two methods, reducing streaking relative to the original images by 89% (B), 85% (G), 84% (R), and 84% (NIR) on average. The maximum streaking reduction was 97% (B), 97% (G), 93% (R), and 84% (NIR), and the standard deviation of streaking was reduced by 88% (B), 86% (G), 83% (R), and 82% (NIR). On average, the streaking reduction achieved by the proposed method surpassed that of the on-orbit statistical method by 21% and that of the laboratory coefficient method by 24% in the B, G, and R bands. The LSD-based method overcorrects in the G and R bands,

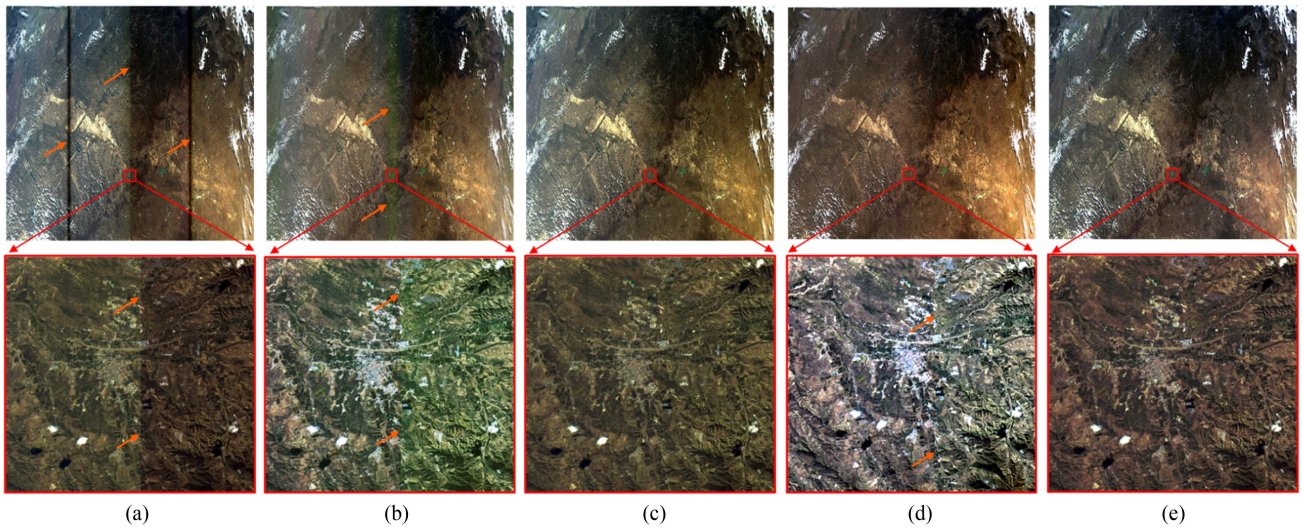

Fig. 20. Before and after relative radiometric correction (RRC) of the HY-1D CZI images of plains scenes. (a) Raw images, (b) images corrected using laboratory coefficient, (c) images corrected using on-orbit statistical, (d) images corrected using LSD method, and (e) images corrected using the proposed method.

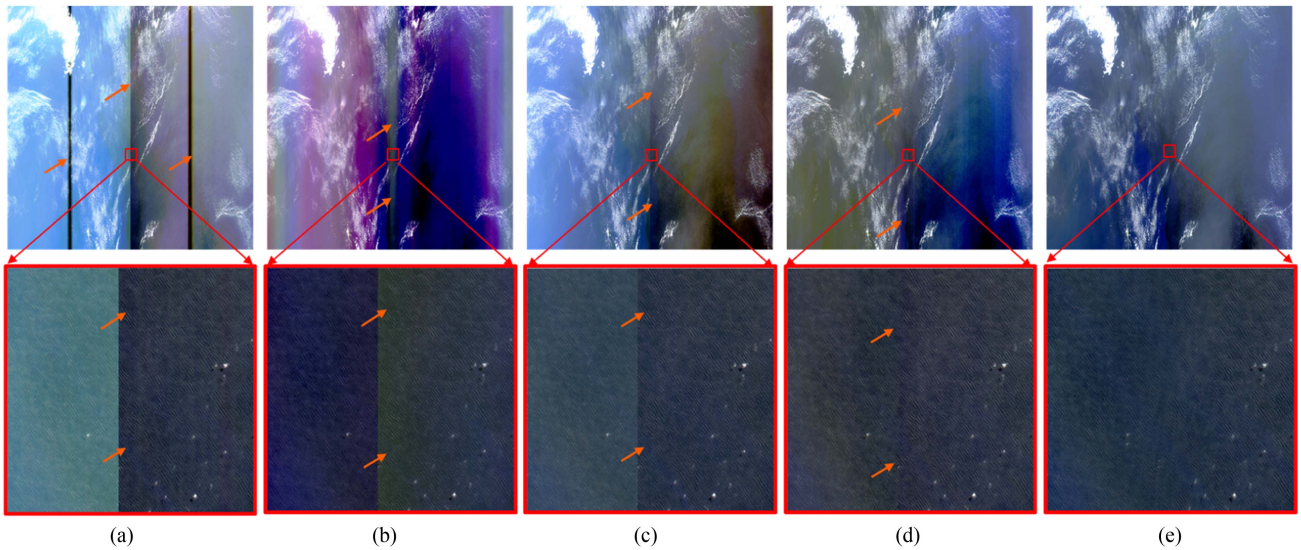

Fig. 21. Before and after RRC of the HY-1D CZI images of sea scenes. (a) Raw images, (b) images corrected using laboratory coefficient, (c) images corrected using on-orbit statistical, (d) images corrected using LSD method, and (e) images corrected using the proposed method.

which clearly leads to noticeable overexposure, as evident from Fig. 25(b) and (c). This results in a lower evaluation value for the average streaking metrics for the LSD-based method, but at the cost of significant detail loss. The clouds and snow on the right side of the image are almost invisible, being entirely overexposed.

For low-frequency stripe noise, the proposed method achieved optimal results in uniform sea and snow scenes. In the sea scenes, relative to the original images, RMS values were reduced by 83% (B), 93% (G), 92% (R), and 89% (NIR). In the snow scenes, the reductions were 73% (B), 77% (G), 68% (R), and 38% (NIR). However, the performance of the laboratory coefficient method was even lower for the G, R, and NIR bands in the sea scenes and lagged noticeably behind the proposed method and the on-orbit statistical method for the G, R, and NIR bands in the snow scenes. Due to the overexposure present in the LSD-based method, its evaluation metrics also fall behind those of the onboard statistics and the proposed method.

Analysis of the quantitative parameters demonstrated consistently superior radiometric calibration quality of the proposed method compared with the laboratory coefficient method across scenes with varying levels of brightness. For high-frequency stripe noise, the correction quality of both the proposed method and the on-orbit statistical method was similar between land and sea scenes, with the proposed method slightly outperforming the on-orbit statistical method for snow scenes. For low-frequency stripe noise, and with respect to the overall color differences in images, the proposed method significantly outperformed the other three methods, as it effectively enhanced image uniformity at the entire scene scale.

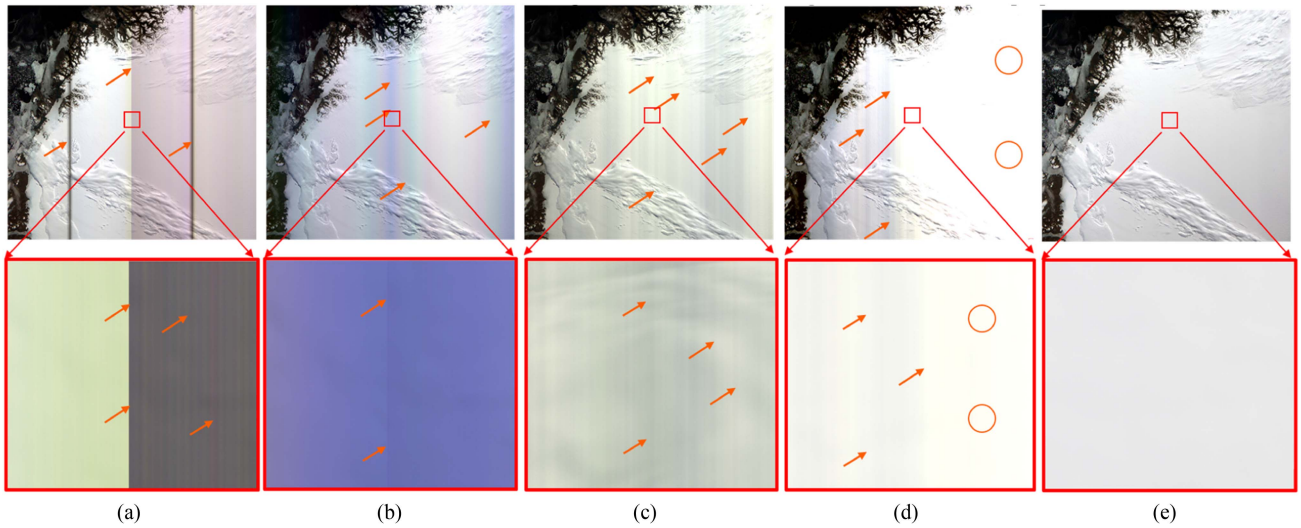

Fig. 22. Before and after RRC of the HY-1D CZI images of snowfield scenes. (a) Raw images, (b) images corrected using laboratory coefficient, (c) images corrected using on-orbit statistical, (d) images corrected using LSD method, and (e) images corrected using the proposed method.

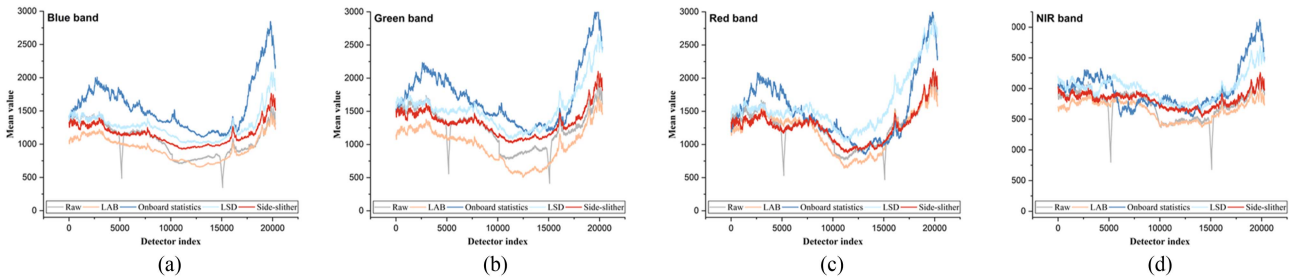

Fig. 23. Distribution of the images' column average DN value for plains scenes. (a) Blue band. (b) Green band. (c) Red band. (d) NIR band.

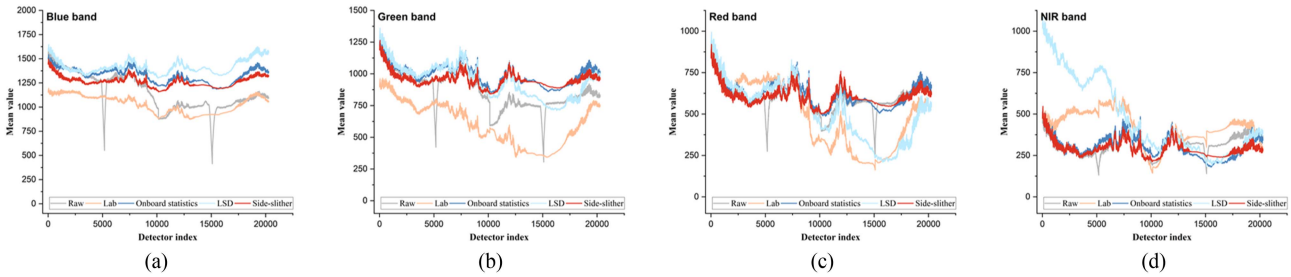

Fig. 24. Distribution of the images' column average DN value for sea scenes. (a) Blue band. (b) Green band. (c) Red band. (d) NIR band.

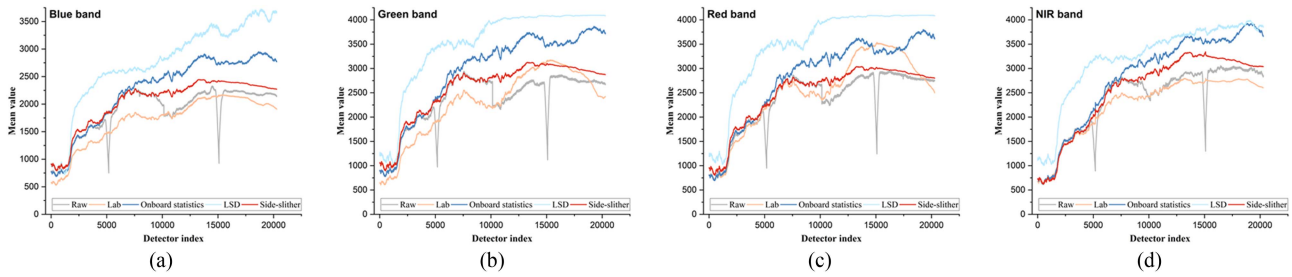

Fig. 25. Distribution of the images' column average DN value for snowfield scenes. (a) Blue band. (b) Green band. (c) Red band. (d) NIR band.

TABLE IV
STEAKING METRICS OF TYPICAL HY-1D CZI PUSH-BROOM IMAGES BEFORE AND AFTER CORRECTION

Data	Band	Streaking_Mean					Streaking_Max					Streaking_Std				
		Raw	laboratory coefficient	Onboard Statistics	LSD	Proposed	Raw	Laboratory coefficient	Onboard Statistics	LSD	Proposed	Raw	Laboratory coefficient	Onboard Statistics	LSD	Proposed
Data-1 Plain	B	0.183	0.048	0.043	0.049	**0.043**	17.099	0.457	0.552	0.659	**0.284**	0.267	0.039	0.035	0.040	**0.035**
	G	0.166	0.090	0.066	0.080	**0.060**	21.087	4.116	**1.829**	2.616	1.863	0.301	0.088	0.055	0.071	**0.050**
	R	0.169	0.096	0.085	0.101	**0.085**	17.837	3.184	**0.756**	1.185	0.886	0.268	0.087	0.068	0.085	**0.068**
	NIR	0.159	0.086	**0.060**	0.067	0.064	17.883	3.472	0.775	1.232	**0.731**	0.254	0.063	**0.049**	0.057	0.053
Data-2 Sea	B	0.188	0.048	**0.046**	0.048	0.046	17.124	0.553	0.559	**0.394**	0.407	0.270	**0.041**	0.043	0.046	0.042
	G	0.182	0.130	0.086	0.106	**0.082**	21.713	3.618	1.079	0.977	**0.663**	0.321	0.122	0.082	0.097	**0.079**
	R	0.205	0.185	0.139	0.217	**0.132**	17.590	15.971	1.072	3.148	**0.993**	0.285	0.226	0.132	0.203	**0.128**
	NIR	0.251	0.228	0.213	**0.154**	0.207	16.678	14.172	3.990	6.903	**2.411**	0.289	0.234	0.203	**0.162**	0.206
Data-3 Snowfield	B	0.225	0.088	0.094	0.097	**0.088**	17.590	0.912	**0.908**	1.102	**0.456**	0.292	0.082	0.088	0.094	**0.033**
	G	0.175	0.073	0.063	**0.037**	0.058	21.373	0.758	0.883	0.632	**0.611**	0.309	0.065	0.061	0.056	**0.043**
	R	0.160	0.050	0.046	**0.025**	0.035	17.439	1.574	1.352	**0.575**	1.120	0.268	0.047	0.049	**0.040**	0.045
	NIR	0.147	0.028	0.029	0.025	**0.018**	16.817	4.117	2.880	**0.914**	2.558	0.257	0.053	0.046	**0.031**	0.044

The bold entities are used to the best indicators.

TABLE V
RMS OF TYPICAL HY-1D CZI PUSH-BROOM IMAGES FOR SEA REGIONS

Data	Band	Mean Column RMS				
		Raw	Laboratory coefficient	Onboard Statistics	LSD	Proposed
Sea Region-1	B	11.829	3.215	2.913	3.705	**1.848**
	G	10.767	9.902	0.861	1.355	**0.610**
	R	10.383	12.815	1.258	2.911	**0.633**
	NIR	10.675	4.651	3.954	16.308	**1.240**
Sea Region-2	B	11.589	3.313	2.958	3.679	**1.956**
	G	10.674	10.630	0.806	1.188	**0.675**
	R	10.261	14.511	1.191	2.996	**0.633**
	NIR	10.563	4.873	4.130	17.243	**1.006**
Sea Region-3	B	11.524	3.239	2.823	3.538	**1.908**
	G	10.583	10.323	0.650	2.001	**1.004**
	R	10.120	14.729	0.913	4.691	**1.009**
	NIR	10.357	4.733	3.453	17.641	**1.415**
Sea Region-4	B	11.713	3.602	3.141	3.833	**2.171**
	G	10.780	13.370	1.216	1.321	**0.591**
	R	10.478	20.325	2.089	6.320	**0.909**
	NIR	11.134	7.505	6.319	21.141	**1.023**

The bold entities are used to the best indicators.

IV. DISCUSSION

The experimental results, as presented in Section III, validate our newly developed method of side-slither data standardization for the HY-1D CZI sensor, with its ultra-WFV and unique arrangement of sensor detectors, as it corrects the curved characteristics of side-slither data effectively. The success of our method can be traced to the approximate free-form arrangement of the sensor detectors in HY-1D CZI, which ensures consistency between the central and edge detectors within the FOV. This arrangement is advantageous in controlling the geometric distortion caused by the large FOV of typical imaging. However, when the detector undergoes 90° rotation for calibration imaging, inconsistencies arise in the effective sizes of detectors in the push-broom direction, distorting the straight-line characteristics in side-slither images. Specifically, this distortion

TABLE VI
RMS OF TYPICAL HY-1D CZI PUSH-BROOM IMAGES FOR SNOW REGIONS

Data	Band	Mean Column RMS				
		Raw	Laboratory coefficient	Onboard Statistics	LSD	Proposed
Snow Region-1	B	8.461	1.946	3.008	8.600	**1.454**
	G	9.929	5.579	3.408	3.139	**1.445**
	R	6.975	6.717	3.423	3.530	**1.435**
	NIR	4.168	5.906	4.794	6.073	**3.103**
Snow Region-2	B	8.423	1.937	3.036	8.592	**1.491**
	G	9.859	5.531	3.489	3.722	**1.428**
	R	6.934	6.634	3.509	4.059	**1.441**
	NIR	4.180	5.743	4.851	5.980	**3.108**
Snow Region-3	B	9.961	2.480	3.008	7.399	3.424
	G	11.368	5.991	3.506	4.466	**3.402**
	R	8.511	6.305	3.703	4.700	**3.477**
	NIR	5.601	5.452	4.631	4.952	**2.858**
Snow Region-4	B	9.599	**1.959**	2.815	7.196	3.406
	G	11.209	4.494	**3.021**	5.208	3.532
	R	8.221	5.874	**3.137**	5.486	3.586
	NIR	5.244	5.678	4.090	4.839	**2.575**

The bold entities are used to the best indicators.

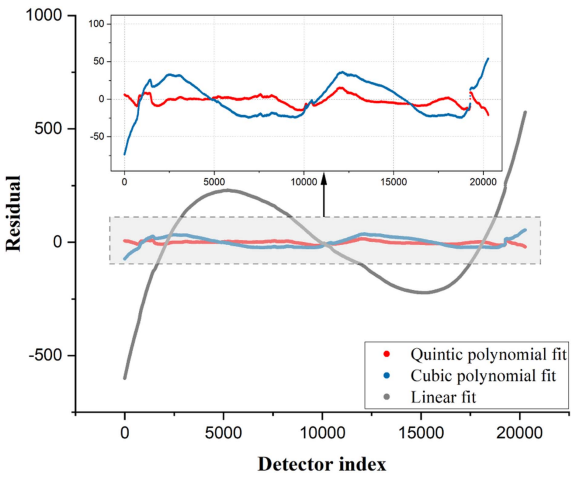

Fig. 26. Distribution of residuals between the first, third, and fifth polynomial fitted values and the true values.

becomes progressively apparent from the center to the edge of the FOV.

The Taylor expansions of (9) can be taken as first, third, fifth, seventh, or even higher terms. To determine the appropriate number of polynomials, the column offset was fitted with the first, third, and fifth terms, and the residuals between each of the fitted values and the true values were calculated (see Fig. 26).

The residuals of the first polynomial fit were significant, with RMSEs up to 199.1; the residuals of the third polynomial fit had RMSEs of up to 22.6; but those of the fifth polynomial were only as high as 5.7; and RMSEs of the seventh and ninth polynomials were even lower, as shown in Table VII. While higher number

TABLE VII
FITTING RESIDUALS OF POLYNOMIALS WITH DIFFERENT TERMS

Term	R-square	RMSE
1	0.4362	199.1030
3	0.9927	22.6103
5	0.9995	5.6607
7	0.9996	5.3197
9	0.9997	4.9276

polynomials more accurately fit the column offset, beyond the fifth polynomial, the R^2 was basically the same such that the fifth polynomial was sufficient to accurately describe the column offset.

Applying both the first-degree polynomial based on the traditional side-slither imaging linear characteristics and a fifth-degree polynomial based on the detector center distance model to the column offset of detector images calculated by (7), as shown in Fig. 27, it can be found that, on both the original images and the images corrected by LSD, the fifth-degree polynomial fitting based on the detector center distance model achieved a higher R^2 value. This means that the method presented in this article is more accurate in describing the side-slither imaging distortion characteristics caused by the nonlinear arrangement of detectors in WFV cameras.

As shown in Fig. 28, by statistically sampling the DN values of typical terrain features corresponding to each sensor's response, we obtain the corresponding distribution of DN values, as shown in Fig. 29. Considering the DN values of clouds in each band, during calibration calculations, the DN values of

TABLE VIII
COMPARISON BETWEEN [38] AND THE PROPOSED METHOD STEAKING METRICS

Data	Band	Streaking_Mean			Streaking_Max			Streaking_Std		
		Raw	[38]	Proposed	Raw	[38]	Proposed	Raw	[38]	Proposed
Plain	B	0.178	0.049	**0.020**	17.304	0.603	**0.109**	0.146	0.040	**0.016**
	G	0.156	0.267	**0.030**	20.964	8.350	**0.597**	0.128	0.205	**0.025**
	R	0.152	0.194	**0.037**	17.766	3.415	**0.244**	0.126	0.133	**0.030**
	NIR	0.147	0.167	**0.024**	17.551	9.180	**0.209**	0.124	0.100	**0.020**

The bold entities are used to the best indicators.

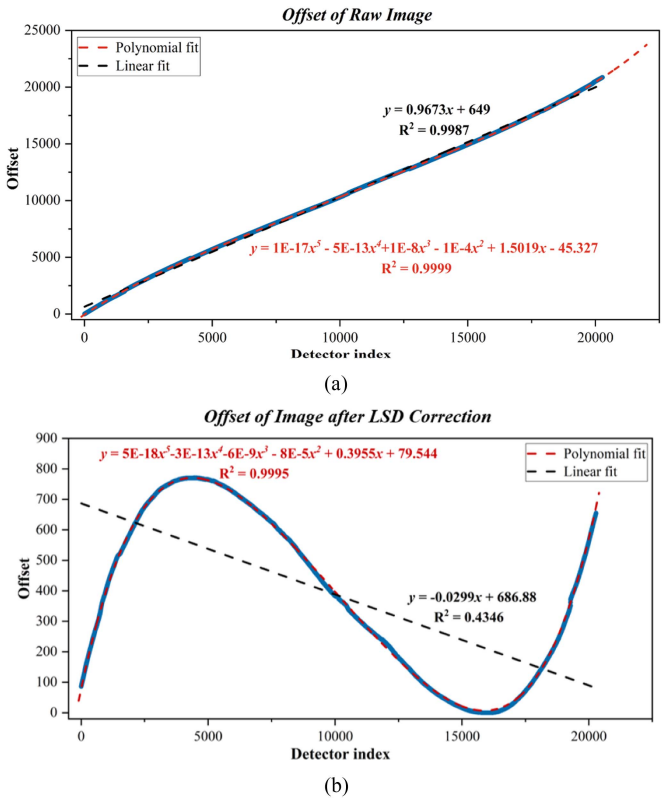

Fig. 27. (a) Column offset of the HY-1D CZI raw image. (b) Column offset of the HY-1D CZI image after LSD correction.

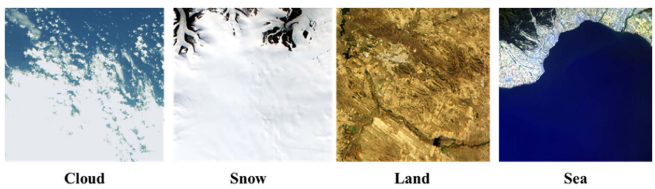

Fig. 28. Schematic of typical terrain features of HY1D-CZI.

clouds are truncated to serve as the upper limit for calculations. The valid calibration DN value ranges, including high response (snow-covered areas), medium response (land), and low response (ocean), are [639, 2850] (B), [570, 3680] (G), [440, 3624] (R), and [210, 3520] (NIR).

At the same time, we selected another track of side-slither data taken during the same period. Based on its distribution of DN values, we produced a DN value heatmap, as shown

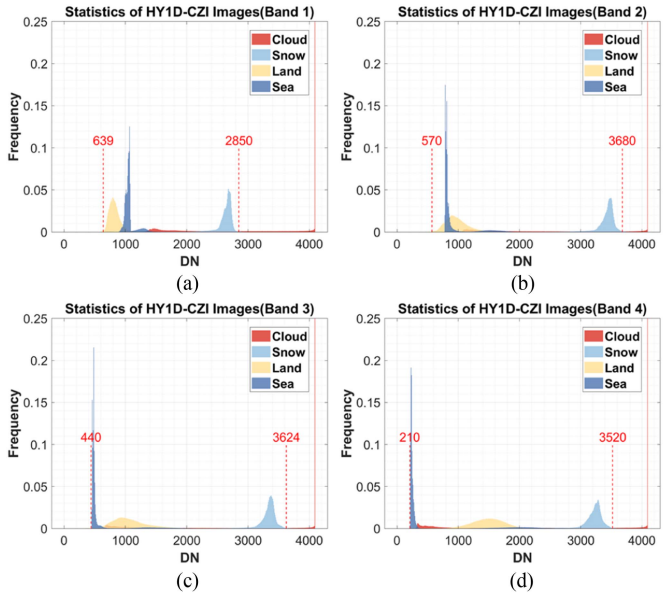

Fig. 29. Distribution of DN value statistics for typical terrain feature sampling of HY1D-CZI.

in Fig. 30. The heat map of DN values shows that most of the data in the B band are below 2500 DN, with the vast majority falling within the effective calibration DN range. In the G band, there are many data points within the 2500–3500 DN range, and some data approach or even reach the upper DN limit (4095). The data in the R band all exceed 3000 DN, with most reaching the DN value limit. Similarly, in the NIR band, a significant amount of data also exceeds the effective calibration range.

After standardization using the LSD correction and the method described in this article, we obtained the corresponding DN value heatmaps, as shown in Fig. 31.

The LSD-based method only selects parts that cover the entire FOV of all CCDs, which first reduces the utilization rate of yaw data, and second, the area covering the entire FOV has many excessively high DN values, often approaching the upper limit of DN values, which can affect the calculation of relative radiometric calibration coefficients. On the other hand, the method described in this article performs yaw data standardization and local relative radiometric coefficient calculations on individual CCDs, followed by global radiometric correction. As shown in Fig. 32, compared with the LSD-based method, this method manages a larger volume of effective DN

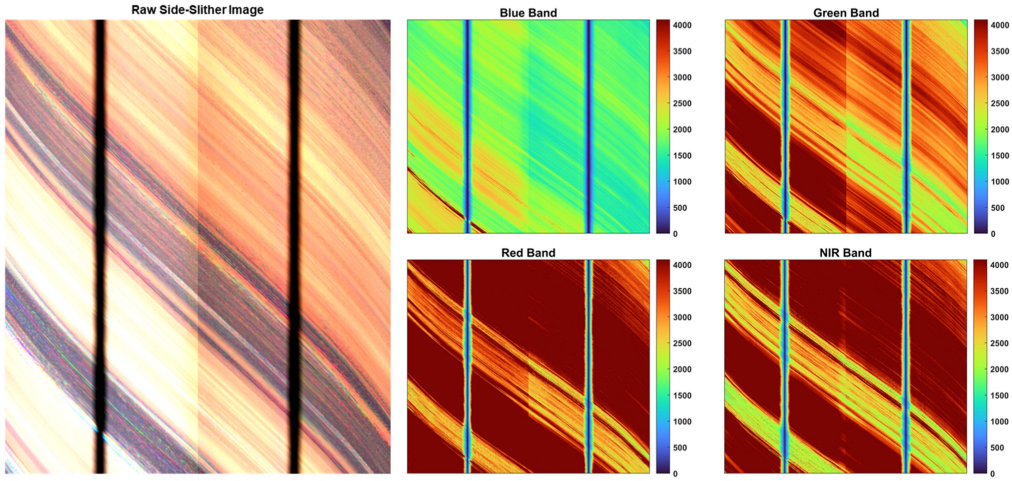

Fig. 30. Heatmap of DN value for side-slither data.

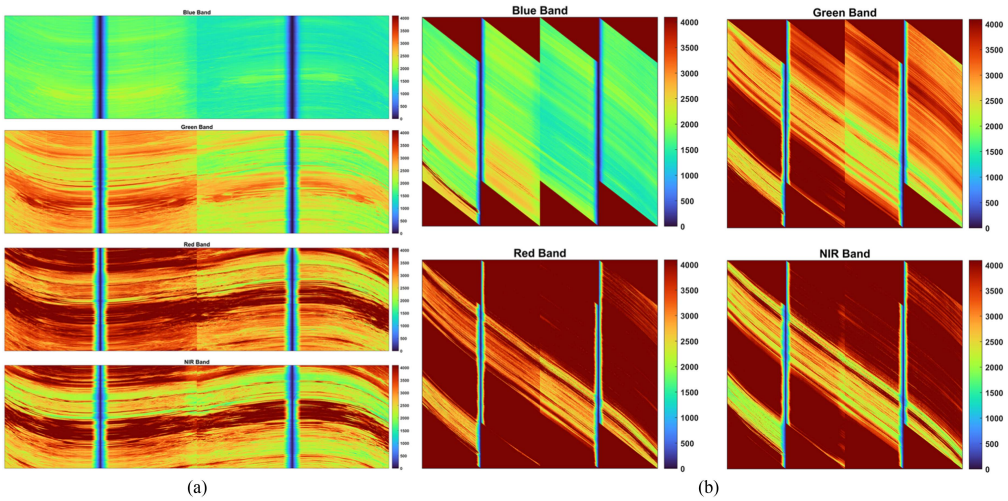

Fig. 31. Heatmap of DN values for side-slither data standardized by (a) LSD-based method and (b) the proposed method.

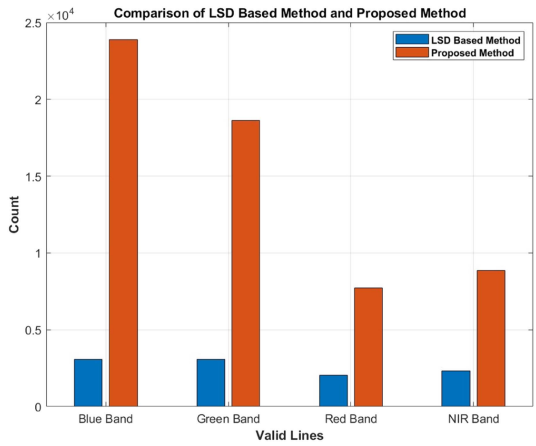

Fig. 32. Proportion of effective DN values in side-slither data using the LSD-based method and the method described in this article.

value data. Due to the lower proportion of effective data in the LSD-based method, the accuracy of the generated radiometric coefficients is lower, resulting in poorer radiometric correction performance compared with the method described in this article. This also explains why the LSD method underperforms in areas of high and low brightness compared with the onboard statistics method and the method described in this article.

Additionally, similar to the LSD-based method, Chen et al. [38] use the parts of the yaw data that cover the entire FOV as calibration data. Although the nonlinear distortion of the yaw data was corrected, as shown in Fig. 15 in Section III-D, the calculation errors of the offsets between adjacent columns and the propagation errors in the column direction led to the appearance of "jaggies" in some parts of the standardized data. The detector central distance model optimizes the fitting of column offsets by establishing a relationship between the detector element numbers and their offsets, achieving the accurate and smooth standardization of yaw data.

Another improvement of the method described in this article lies in the increase in the volume of effective calibration data involved in the standardization of yaw images. Since the original yaw images in the G and R bands contain a large amount of

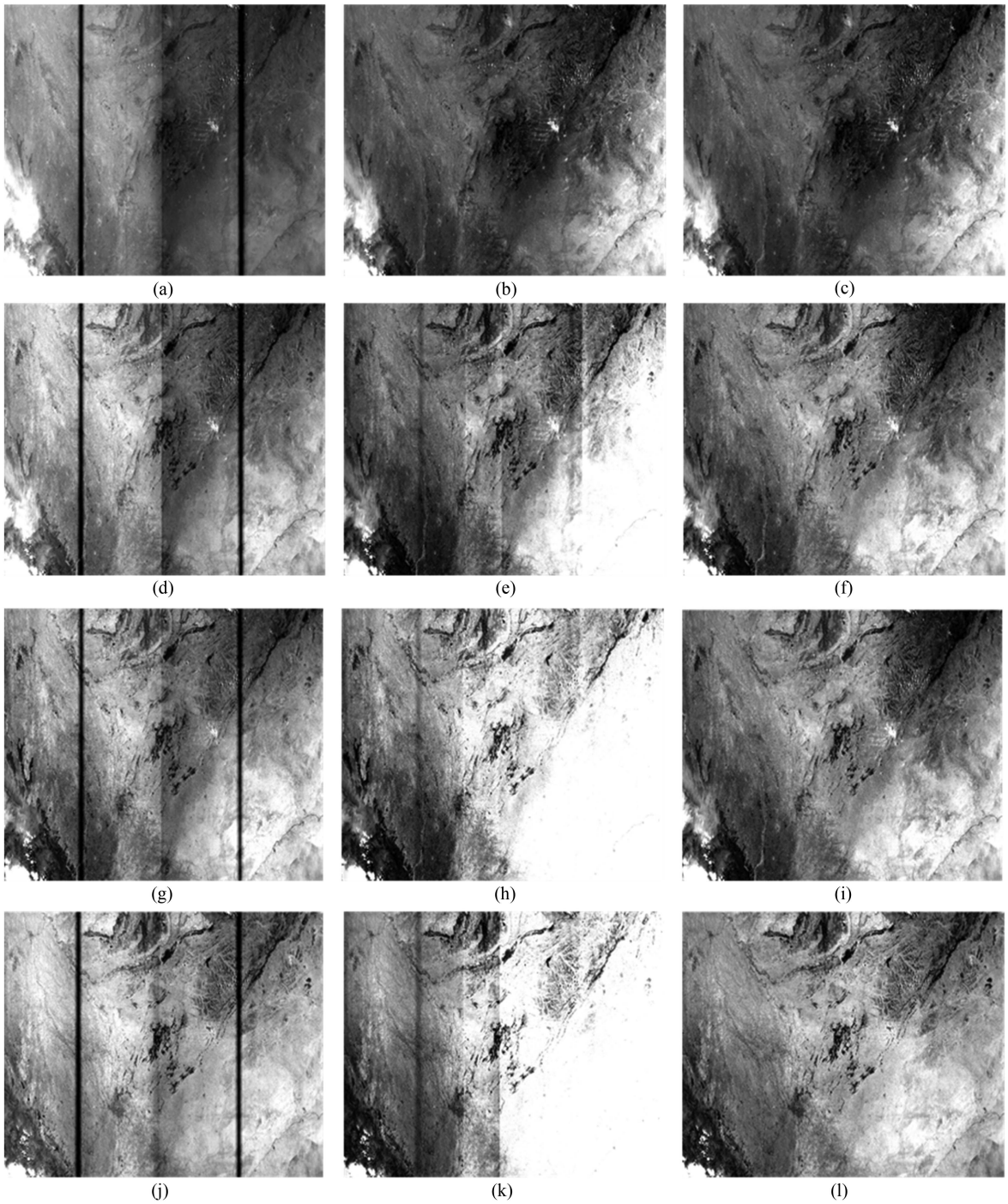

Fig. 33. Before and after RRC of the HY-1D CZI images. (a), (d), (g), and (j) Raw images in blue band, green band, red band, and NIR band, respectively. (b), (e), (h), and (k) Images corrected using column offset calculation method in blue band, green band, red band, and NIR band, respectively. (c), (f), (i), and (l) Images corrected using the proposed method in blue band, green band, red band, and NIR band, respectively.

data exceeding the effective calibration DN value range, using only data covering the entire FOV results in lower precision of relative radiometric calibration coefficients in the G and R bands. Accordingly, we used the method from the article [38] and the improved method described in this article for experimental comparison.

Fig. 33 and Table VIII clearly shows that the literature [38] used only the column offset calculation to standardize yaw images and calculate relative radiometric calibration coefficients. In the B band, it achieved nearly the same effect as the method described in this article, but it performed poorly in the G, R, and NIR bands. The corrected images show obvious striping flaws, and the right half of the image is noticeably overexposed. In contrast, the method described in this article achieves good correction results across all four bands. This demonstrates that our approach significantly improves the utilization of side-slither data and avoids the distortion of radiometric correction parameters caused by insufficient inclusion of side slither in

the calculations, increasing the number of effective calibration DN values and enhancing the precision of relative radiometric calibration.

In both the visual assessment and the quantitative evaluation, the results from the experiments on typical push-broom imaging clearly demonstrated the exceptional performance of our approach. Typically, land and ocean scenes are of greatest interest for CZI imaging, and they are the primary focus of typical imaging plans. The calibration quality of the on-orbit statistical method is contingent on the duration of the period over which statistical data accumulate. In this experiment, the on-orbit statistical method utilized six months of accumulated statistical data, resulting in excellent correction outcomes for both ocean and land scenes. Our method achieved nearly identical results for the land scene and slightly better results for the ocean scene. In scenes characterized by fewer statistical samples, such as snow-covered areas, significantly better visual effects and evaluation metrics were obtained with our method than with the on-orbit statistical method. This underscores the capacity of our method to yield satisfactory radiometric correction results across low-, medium-, and high-range radiance levels.

By contrast, the comparative experiments involving the LSD method revealed the limitations inherent to the classical side-slither RRC approach. The LSD method's reliance on capturing side-slither data by sweeping across the entire FOV creates challenges when applied to CZI, given its WFV characteristics. The truncated side-slither data lack comprehensive coverage of the sensor's dynamic range, and the side-slither data standardization method based on the linear features fails to effectively rectify the curved characteristics within those data. Consequently, the radiometric correction results derived from the LSD method exhibited notably weaker visual effects and evaluation metrics than those obtained with either the on-orbit statistical method or our proposed method.

Following advances in remote-sensing satellite technology, an increasing number of satellites are now equipped with agile imaging capabilities, allowing sensor RRC during on-orbit operations through the 90° side-slither imaging mode. However, as a result, applying classical methods directly from the field to conduct RRC for satellite sensors with varying FOV sizes and structural characteristics is no longer suitable. Instead, calibration methods and strategies tailored to the unique attributes of satellite sensors are needed. By addressing the specific structural features of HY-1D CZI, we developed an RRC method based on side-slither data that achieves high-precision ultra-WFV sensors, such as the HY-1D CZI. The proposed offset calculation method based on the adjacent column RMSE and the model describing side-slither data curve characteristics can be extended to other satellites, provided that their structural attributes are considered, thus enabling high-precision side-slither data standardization and, in turn, high-quality RRC coefficients.

V. Conclusion

By analyzing the structural characteristics of the HY-1D CZI sensor, we developed a side-slither data RRC method suitable for ultra-WFV sensors with a nonflat detector arrangement. The main contributions of our work are given as follows.

1) We developed a polynomial correction model based on a thorough analysis of the unique structural traits of WFV push-broom optical cameras, enabling precise standardization of the nonlinear distortions in side-slither data arising from nonflat detector arrangement.
2) The overlapping information of multiple CCDs within the camera was used to devise a strategy for local-to-global side-slither calibration, which obviates the requirement for the corresponding pixels in calibration data to cover the entire FOV.

We verified our method on HY-1D CZI, and the validation data were captured over three locations: Greenland, North China Plain, and the Philippine Sea, including snowfields, land, and ocean, thus allowing verification of the radiometric calibration performance across high-, medium-, and low-sensor DN values. The experimental results reveal the effectiveness of our method in rectifying nonlinear distortions in side-slither data and evidenced reduction in stripe artifacts and RMS compared with classical side-slither methods and on-orbit statistical methods. These results demonstrated that our method significantly improves the relative radiometric quality of HY-1D CZI, thus providing a robust method for RRC in WFV push-broom optical satellites.

References

[1] X. Xiong and W. Barnes, "An overview of modis radiometric calibration and characterization," *Adv. Atmos. Sci.*, vol. 23, no. 1, pp. 69–79, 2006, doi: 10.1007/s00376-006-0008-3.

[2] Y. Duan, L. Yan, B. Yang, X. Jing, and W. Chen, "Outdoor relative radiometric calibration method using gray scale targets," *Sci. China Technol. Sci.*, vol. 56, no. 7, pp. 1825–1834, 2013, doi: 10.1007/s11431-013-5230-5.

[3] L. Zhang, C. Huang, T. Wu, F. Zhang, and Q. Tong, "Laboratory calibration of a field imaging spectrometer system," *Sensors*, vol. 11, no. 3, pp. 2408–2425, 2011, doi: 10.3390/s110302408.

[4] M. Shimada, H. Oaku, H. Oguma, R. O. Green, Y. Miyachi, and H. Shimoda, "Calibration of advanced visible and near infrared radiometer," *IEEE Trans. Geosci. Remote Sens.*, vol. 37, no. 3, pp. 1472–1483, May 1999, doi: 10.1109/36.763260.

[5] M. Pagnutti et al., "Radiometric characterization of IKONOS multispectral imagery," *Remote Sens. Environ.*, vol. 88, no. 1/2, pp. 53–68, 2003, doi: 10.1016/j.rse.2003.07.008.

[6] R. Bindschadler and H. Choi, "Characterizing and correcting hyperion detectors using ice-sheet images," *IEEE Trans. Geosci. Remote Sens.*, vol. 41, no. 6, pp. 1189–1193, Jun. 2003, doi: 10.1109/tgrs.2003.813208.

[7] E. Knight and G. Kvaran, "Landsat-8 operational land imager design, characterization and performance," *Remote Sens.*, vol. 6, no. 11, pp. 10286–10305, 2014, doi: 10.3390/rs61110286.

[8] B. K. P. Horn and R. J. Woodham, "Destriping Landsat MSS images by histogram modification," *Comput. Graph. Image Process.*, vol. 10, no. 1, pp. 69–83, 1979, doi: 10.1016/0146-664x(79)90035-2.

[9] D. Helder, S. Hijazi, and T. Ruggles, "A radiometric evaluation of the advanced land imager," in *Proc. IEEE Int. Geosci. Remote Sens. Symp.*, 2002, vol. 1, pp. 576–578, doi: 10.1109/igarss.2002.1025110.

[10] A. Moghimi, T. Celik, and A. Mohammadzadeh, "Tensor-based keypoint detection and switching regression model for relative radiometric normalization of bitemporal multispectral images," *Int. J. Remote Sens.*, vol. 43, no. 11, pp. 3927–3956, Jun. 2022, doi: 10.1080/01431161.2022.2102951.

[11] S. Kabir, L. Leigh, and D. Helder, "Vicarious methodologies to assess and improve the quality of the optical remote sensing images: A critical review," *Remote Sens.*, vol. 12, no. 24, Dec. 2020, Art. no. 4029, doi: 10.3390/rs12244029.

[12] L. Feng et al., "Radiometric cross-calibration of Gaofen-1 WFV cameras using Landsat-8 OLI images: A solution for large view angle associated problems," *Remote Sens. Environ.*, vol. 174, pp. 56–68, Mar. 2016, doi: 10.1016/j.rse.2015.11.031.

[13] L. G. Denaro and C.-H. Lin, "Hybrid canonical correlation analysis and regression for radiometric normalization of cross-sensor satellite imagery," *IEEE J. Sel. Topics Appl. Earth Observ. Remote Sens.*, vol. 13, pp. 976–986, Feb. 2020, doi: 10.1109/jstars.2020.2971857.
[14] T. Choi, X. Xiong, and Z. Wang, "On-orbit lunar modulation transfer function measurements for the moderate resolution imaging spectroradiometer," *IEEE Trans. Geosci. Remote Sens.*, vol. 52, no. 1, pp. 270–277, Jan. 2014, doi: 10.1109/tgrs.2013.2238545.
[15] M. Shrestha, L. Leigh, and D. Helder, "Classification of North Africa for use as an extended pseudo invariant calibration sites (EPICS) for radiometric calibration and stability monitoring of optical satellite sensors," *Remote Sens.*, vol. 11, no. 7, Apr. 2019, Art. no. 875, doi: 10.3390/rs11070875.
[16] W. Bonnet and T. Celik, "Random sampling-based relative radiometric normalization," *IEEE Geosci. Remote Sens. Lett.*, vol. 19, 2022, Art. no. 8005704, doi: 10.1109/lgrs.2020.3047344.
[17] J. Geng, W. Gan, J. Xu, R. Yang, and S. Wang, "Support vector machine regression (SVR)-based nonlinear modeling of radiometric transforming relation for the coarse-resolution data-referenced relative radiometric normalization (RRN)," *Geo-Spatial Inf. Sci.*, vol. 23, no. 3, pp. 237–247, Jul. 2020, doi: 10.1080/10095020.2020.1785958.
[18] K. Liu, T. Ke, P. Tao, J. He, K. Xi, and K. Yang, "Robust radiometric normalization of multitemporal satellite images via block adjustment without master images," *IEEE J. Sel. Topics Appl. Earth Observ. Remote Sens.*, vol. 13, pp. 6029–6043, Oct. 2020, doi: 10.1109/jstars.2020.3028062.
[19] X. Zhang, R. Feng, X. Li, H. Shen, and Z. Yuan, "Block adjustment-based radiometric normalization by considering global and local differences," *IEEE Geosci. Remote Sens. Lett.*, vol. 19, 2022, Art. no. 8002805, doi: 10.1109/lgrs.2020.3031398.
[20] B. G. Henderson and K. S. Krause, "Relative radiometric correction of QuickBird imagery using the side-slither technique on orbit," *Proc. SPIE*, vol. 5542, pp. 426–436, Oct. 2004, doi: 10.1117/12.559910.
[21] P. Kubik and V. Pascal, "Amethist: A method for equalization thanks to histograms," *Proc. SPIE*, vol. 5570, pp. 256–267, Nov. 2004, doi: 10.1117/12.565091.
[22] G. Blanchet et al., "Pleiades-HR innovative techniques for radiometric image quality commissioning," *Int. Arch. Photogramm., Remote Sens. Spatial Inf. Sci.*, vol. XXXIX-B1, pp. 513–518, 2012, doi: 10.5194/isprsarchives-xxxix-b1-513-2012.
[23] C. Chen, J. Pan, M. Wang, and Y. Zhu, "Side-slither data-based vignetting correction of high-resolution spaceborne camera with optical focal plane assembly," *Sensors*, vol. 18, no. 10, 2018, Art. no. 3402, doi: 10.3390/s18103402.
[24] M. Wang, C. Chen, J. Pan, Y. Zhu, and X. Chang, "A relative radiometric calibration method based on the histogram of side-slither data for high-resolution optical satellite imagery," *Remote Sens.*, vol. 10, no. 3, 2018, Art. no. 381, doi: 10.3390/rs10030381.
[25] F. Pesta, S. Bhatta, D. Helder, and N. Mishra, "Radiometric non-uniformity characterization and correction of Landsat 8 OLI using Earth imagery-based techniques," *Remote Sens.*, vol. 7, no. 1, pp. 430–446, 2014, doi: 10.3390/rs70100430.
[26] C. Begeman, D. Helder, L. Leigh, and C. Pinkert, "Relative radiometric correction of pushbroom satellites using the yaw maneuver," *Remote Sens.*, vol. 14, no. 12, 2022, Art. no. 2820, doi: 10.3390/rs14122820.
[27] G. Zhang and L. Li, "A study on relative radiometric calibration without calibration field for YG-25," *Acta Geodaetica et Cartographica Sinica*, vol. 46, no. 8, pp. 1009–1016, 2017.
[28] A. Gerace, J. Schott, M. Gartley, and M. Montanaro, "An analysis of the side slither on-orbit calibration technique using the DIRSIG model," *Remote Sens.*, vol. 6, no. 11, pp. 10523–10545, 2014, doi: 10.3390/rs61110523.
[29] L. Li, G. Zhang, Y. Jiang, and X. Shen, "An improved on-orbit relative radiometric calibration method for agile high-resolution optical remote-sensing satellites with sensor geometric distortion," *IEEE Trans. Geosci. Remote Sens.*, vol. 60, 2022, Art. no. 5606715, doi: 10.1109/tgrs.2021.3078815.
[30] J. Pan, M. Wang, D. Li, and J. Li, "A network-based radiometric equalization approach for digital aerial orthoimages," *IEEE Geosci. Remote Sens. Lett.*, vol. 7, no. 2, pp. 401–405, Apr. 2010, doi: 10.1109/lgrs.2009.2037442.
[31] J. Pan, M. Wang, D. Li, and J. Li, "Automatic generation of seamline network using area Voronoi diagrams with overlap," *IEEE Trans. Geosci. Remote Sens.*, vol. 47, no. 6, pp. 1737–1744, Jun. 2009, doi: 10.1109/tgrs.2008.2009880.
[32] L. Yu, Y. Zhang, M. Sun, X. Zhou, and C. Liu, "An auto-adapting global-to-local color balancing method for optical imagery mosaic," *ISPRS J. Photogramm. Remote Sens.*, vol. 132, pp. 1–19, 2017, doi: 10.1016/j.isprsjprs.2017.08.002.
[33] M. Wegener, "Destriping multiple sensor imagery by improved histogram matching," *Int. J. Remote Sens.*, vol. 11, no. 5, pp. 859–875, 1990, doi: 10.1080/01431169008955060.
[34] V. Sadeghi, H. Ebadi, and F. F. Ahmadi, "A new model for automatic normalization of multitemporal satellite images using artificial neural network and mathematical methods," *Appl. Math. Model.*, vol. 37, no. 9, pp. 6437–6445, 2013, doi: 10.1016/j.apm.2013.01.006.
[35] C. Song, C. E. Woodcock, K. C. Seto, M. P. Lenney, and S. A. Macomber, "Classification and change detection using Landsat TM data," *Remote Sens. Environ.*, vol. 75, no. 2, pp. 230–244, 2001, doi: 10.1016/s0034-4257(00)00169-3.
[36] A. Eivazi, A. Kolesnikov, V. Junttila, and T. Kauranne, "Variance-preserving mosaicing of multiple satellite images for forest parameter estimation: Radiometric normalization," *ISPRS J. Photogramm. Remote Sens.*, vol. 105, pp. 120–127, 2015, doi: 10.1016/j.isprsjprs.2015.03.007.
[37] X. Li, N. Hui, H. Shen, Y. Fu, and L. Zhang, "A robust mosaicking procedure for high spatial resolution remote sensing images," *ISPRS J. Photogramm. Remote Sens.*, vol. 109, pp. 108–125, 2015, doi: 10.1016/j.isprsjprs.2015.09.009.
[38] R. Chen et al., "A study on relative radiometric calibration using side-slither data for Hy-1D Czi," *Nat. Remote Sens. Bull.*, vol. 27, no. 1, pp. 43–54, 2023, doi: 10.11834/jrs.20221611.
[39] K. S. Krause, "QuickBird relative radiometric performance and on-orbit long term trending," in *Proc. SPIE*, vol. 6296, pp. 231–242, Aug. 2006, doi: 10.1117/12.679693.
[40] L. Li et al., "On-orbit relative radiometric calibration of the Bayer pattern push-broom sensor for Zhuhai-1 video satellites," *Remote Sens.*, vol. 15, no. 2, 2023, Art. no. 377, doi: 10.3390/rs15020377.
[41] T. Peng, Y. Pi, R. Chen, J. Pan, J. Cai, and M. Wang, "A combined side-slither relative radiometric calibration method for non-collinear TDI-CCDS," *IEEE Geosci. Remote Sens. Lett.*, vol. 20, Sep. 2023, Art. no. 5509905, doi: 10.1109/lgrs.2023.3314511.

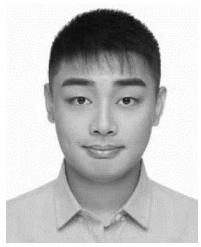

Ru Chen was born in 1995. He received the B.Eng. degree in photogrammetry and remote sensing and the M.Sc. degree in surveying and mapping engineering in 2017 and 2019, respectively, from Wuhan University, Wuhan, China, where he is currently working toward the Ph.D. degree in photogrammetry and remote sensing with the State Key Laboratory of Information Engineering in Surveying, Mapping and Remote Sensing.

His research interests include radiometric calibration and processing of spaceborne optical imagery.

Mi Wang (Member, IEEE) received the B.Eng., M.Sc., and Ph.D. degrees in photogrammetry and remote sensing from Wuhan University, Wuhan, China, in 1997, 1999, and 2001, respectively.

Since 2008, he has been a Professor with the State Key Laboratory of Information Engineering in Surveying, Mapping, and Remote Sensing, Wuhan University. His research interests include the measurable seamless stereo orthoimage databases, geographic information systems, and high-precision remote sensing image processing.

Yingdong Pi was born in Mingshui County, Heilongjiang Province, China, in 1992. He received the B.Eng., M.Sc., and Ph.D. degrees in photogrammetry and remote sensing from Wuhan University, Wuhan, China, in 2014, 2017, and 2021, respectively.

He is currently a Postdoctoral Fellow with the State Key Laboratory of Information Engineering in Surveying, Mapping, and Remote Sensing, Wuhan University. His research interests include high-precision remote sensing image processing and deep space detection.

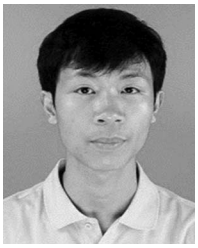

Tao Peng was born in 1997. He received the M.A. degree in photogrammetry and remote sensing in 2022 from the State Key Laboratory of Information Engineering in Surveying, Mapping and Remote Sensing, Wuhan University, Wuhan, China, where he is currently working toward the Ph.D. degree in photogrammetry and remote sensing.

His research interests include relative radiometric calibration and normalization, and remote sensing imagery denoising.

Rongfan Dai received the B.S. and M.S. degrees in geodetection and information technology from the China University of Geosciences, Wuhan, China, in 2013 and 2017, respectively. He is currently working toward the Ph.D. degree in electronic and information engineering with Wuhan University, Wuhan, China.

His research interests include high-precision remote sensing image processing and information intelligent extraction.

Ru Wang received the B.Sc. degree in surveying and mapping engineering from Southeast University, Nanjing, China, in 2017. She is currently working toward the Ph.D. degree in photogrammetry and remote sensing with Wuhan University, Wuhan, China.

Her research interests include the remote sensing image processing, deep learning, and InSAR technique.